Towards filtered drag force model for non-cohesive and cohesive particle-gas flows

Towards filtered drag force model for non-cohesive and cohesive particle-gas flows

Ali Ozel, Yile Gu, Christian C. Milioli, Jari Kolehmainen, and Sankaran Sundaresan

Citation: Physics of Fluids **29**, 103308 (2017);
View online: https://doi.org/10.1063/1.5000516
View Table of Contents: http://aip.scitation.org/toc/phf/29/10
Published by the American Institute of Physics

Towards filtered drag force model for non-cohesive and cohesive particle-gas flows

Ali Ozel,[a] Yile Gu, Christian C. Milioli, Jari Kolehmainen, and Sankaran Sundaresan
Department of Chemical and Biological Engineering, Princeton University, Princeton, New Jersey 08544, USA

(Received 16 August 2017; accepted 13 October 2017; published online 31 October 2017)

Euler-Lagrange simulations of gas-solid flows in unbounded domains have been performed to study sub-grid modeling of the filtered drag force for non-cohesive and cohesive particles. The filtered drag forces under various microstructures and flow conditions were analyzed in terms of various sub-grid quantities: the sub-grid drift velocity, which stems from the sub-grid correlation between the local fluid velocity and the local particle volume fraction, and the scalar variance of solid volume fraction, which is a measure to identify the degree of local inhomogeneity of volume fraction within a filter volume. The results show that the drift velocity and the scalar variance exert systematic effects on the filtered drag force. Effects of particle and domain sizes, gravitational accelerations, and mass loadings on the filtered drag are also studied, and it is shown that these effects can be captured by both sub-grid quantities. Additionally, the effect of cohesion force through the van der Waals interaction on the filtered drag force is investigated, and it is found that there is no significant difference on the dependence of the filtered drag coefficient of cohesive and non-cohesive particles on the sub-grid drift velocity or the scalar variance of solid volume fraction. The assessment of predictabilities of sub-grid quantities was performed by correlation coefficient analyses in *a priori* manner, and it is found that the drift velocity is superior. However, the drift velocity is not available in "coarse-grid" simulations and a specific closure is needed. A dynamic scale-similarity approach was used to model drift velocity but the predictability of that model is not entirely satisfactory. It is concluded that one must develop a more elaborate model for estimating the drift velocity in "coarse-grid" simulations. *Published by AIP Publishing.* https://doi.org/10.1063/1.5000516

I. INTRODUCTION

Industrial-scale fluidized beds where particles are converted from a solid-like state to a fluid-like state by an up-flow of gas provide uniform temperature distribution and mixing, which are beneficial for many chemical processes. These beds typically operate in the turbulent fluidization regime or in the circulating fluidized bed mode, where particles and gases are transported up at high velocities through large vessels. These flows exhibit a wide range of temporal and spatial scales; the spatial structures range from a few particle diameters to the scale of the vessel. This multi-scale nature of the flow emerges through intrinsic instabilities associated with fluidization that arise even in regions far away from the boundaries. This intrinsic instability produces bubble-like voids at high particle concentrations and particle clusters and streamers at low particle concentrations,[1] which coalesce and breakup to yield multi-scale structures. Such hydrodynamically driven structures are further modified by inter-particle cohesion through the van der Waals interaction in fluidization of Geldart group A particles.[2,3]

The Euler-Euler approach is commonly used to simulate gas-solid flows in industrial-scale fluidized beds. In this approach, solid and fluid phases are modeled as interpenetrating continua[4] and solid phase transport properties such as pressure and viscosity are modeled via the kinetic theory of granular flows.[5–11] To accurately predict the hydrodynamics of beds, the computational grid size for Euler-Euler simulations should be smaller than the sizes of particle clusters,[12–14] which can be as small as a few particle diameters.[15] In particular, the inability to capture the effect of inhomogeneity on small length scales leads to inadequate modeling of the momentum, species, and heat transfer between phases and solid phase stresses. Although the Euler-Euler approach has been applied successfully to resolve the particle clustering effect in small computational domains,[16–18] simulations with highly resolved grids are not affordable for industrial applications due to computational costs. To overcome this problem, a filtered Euler-Euler approach is being developed to simulate large-scale flow problems.[12,14,19–24] In the filtered Euler-Euler approach, the filtered transport equations for solid and fluid phases are solved on the "coarse-grid" (i.e., the computational mesh resolution is not sufficient enough to resolve the particle clustering effect at small scales), and the effect of unresolved structures is taken into account via sub-grid modeling. The filtered transport equations are derived from the standard Euler-Euler transport equations through volume-averaging[14] in which sub-grid correlations arise. Previous studies have shown that the sub-grid correction to the drag term is the most significant one and if it is not accounted for in coarse-grid simulations, the resolved drag is over-predicted.[14,19,21,23] As a secondary effect, large-scale solid velocity fluctuations play a role on the redistribution of particles.[14,22,24,25]

[a]aozel@princeton.edu

The modeling attempts for the sub-grid contribution of the drag term fall into two categories. The first category models use filtered quantities explicitly available in filtered model simulations: for instance, Igci and Sundaresan[20] expressed the filtered drag force as a function of the filtered volume fraction and the filter size. Later studies have sought to include the filtered relative velocity as an additional marker.[22,23,26] In the second category, proposed models use sub-grid quantities such as the drift velocity and the scalar variance of solid volume fraction which are not available in filtered model simulations. A functional model proposed by Parmentier *et al.*[21] for the drift velocity accurately predicted the bed height in a 2-D dense fluidized bed. As a continuation work of Parmentier *et al.*,[21] Ozel *et al.*[14] showed that the drift velocity must be accounted for the accurate estimation of solid flux in a 3-D dilute periodic channel flow. Recently, Schneiderbauer[24] employed the scalar variance of solid volume fraction and large-scale velocity fluctuations of the gas and particle phases as markers. In these approaches, an additional level of modeling is necessary to estimate the sub-grid quantities.

Aforementioned studies are limited to hydrodynamics of gas-solid flows with non-cohesive mono-disperse particles. However, accurate constitutive models for the Euler-Euler approaches have not been developed for particles with complex interactions such as liquid bridges between particles, cohesion or repulsion due to electrostatic charges carried by the particles, and cohesion through the van der Waals interaction. The derivation of Euler-Euler models with complex particle physics is challenging, and theoretical development of these models posits binary and instantaneous interactions between particles and does not consider enduring interaction which is typical in complex systems. In contrast, numerous Euler-Lagrange models, where the locally averaged equations of motion for the fluid phase are solved in an Eulerian framework and the particles are tracked in a Lagrangian fashion by solving Newton's equations of motion, have been successfully used to simulate gas-solid flows with such complex interactions.[27–35] Instead of incorporating complex particle physics into Euler-Euler models via theoretical derivations, it is more straightforward to perform Euler-Lagrange simulations including complex particle physics and use these simulation results to directly propose constitutive relations for filtered Euler-Euler models. As shown in our previous study,[36] one can use the drag corrections deduced from Euler-Lagrange simulations for filtered Euler-Euler simulations. In the present study, we have performed Euler-Lagrange simulations of gas-solid flows in unbounded (fully periodic) domains with and without cohesive force to deduce the effective drag force model. Cohesion arises from the van der Waals force[37] and we varied the cohesion level by adjusting the Hamaker constant. We have also performed simulations with different particle and domain sizes, gravitational accelerations, and mass loadings (domain-averaged solid volume fractions). The simulation results allow us to address the following questions:

- Is there any key sub-grid quantity for the filtered drag force modeling that emerges similarly for different domain sizes, mass loadings, and particle Reynolds and Froude numbers?
- What is the relative importance of particle cohesion on the extent of correction to the drag law for coarse-grained Euler-Lagrange and filtered Euler-Euler approaches?
- How well can one estimate the key sub-grid quantities used for the filtered drag force modeling in coarse-grid simulations?

This paper is organized as follows. We first present the flow configuration in Sec. II. The filtering procedure is described in Sec. III. In Sec. IV, the filtered results are presented. In Sec. V, the model assessments are given. Finally, the principal results are summarized in Sec. VI.

II. FLOW CONFIGURATION

The gas phase equations are solved using an OpenFOAM-based Computational Fluid Dynamics (CFD) solver,[38] while the particle phase discrete element method (DEM) equations are evolved via the LIGGGHTS platform.[39] The two phases are coupled via an open-source software CFDEMcoupling.[40,41] The public version of CFDEMcoupling has been modified to be capable of performing simulations with hundred million particles by Ozel *et al.*[36] A full description of the equations used for the CFD and DEM aspects of the simulation is provided in Appendix A.

DEM[42] was used to model particle-particle interactions and the motion of each individual particle. Newton's equations of motion were solved by the velocity-Verlet algorithm[43] with second order accuracy in time. A Hertzian spring model was used for normal and tangential contacts allowing for inelastic collisions and Coulomb friction for particle-particle interactions. The particles were simulated as being less stiff than they are in reality, to avoid the need to use small time steps. The DEM parameters and particle properties used are summarized in Table I. The properties are typical of fluid catalytic cracking particles.[44–46]

We model the gas phase as a continuum, with a discretized form of the volume-averaged fluid equations[4] used to solve for gas velocity and pressure on a co-located fluid grid. For the time-integration of momentum equations of gas phase, an Euler scheme with first order accuracy in time and a central-upwind scheme for the spatial discretization of the equations were used. The grid spacing was 3 d_p, which was sufficient for accurate and grid-independent simulation results.[47] The gas phase properties are summarized in Table I.

Simulations were performed for various domain-averaged solid volume fractions, three different particle sizes, two different gravity accelerations, and two different Hamaker constants. The simulation parameters in dimensionless forms are given in Table I. The particle Reynold number Re_p based on the terminal velocity of a particle varies from 0.32 to 33.23. Particles are highly inertial and the particle Stoke number St_p varies from 65 to 799. The simulations were performed over a particle Froude number Fr_p range of 20–2130. The cohesion force through the van der Waals interaction was only accounted for simulations with Geldart group A type particles[2] ($d_p = 75$ μm). The particle Bond number Bo_p is defined as the ratio of maximum cohesive force and particle weight.

TABLE I. Computational domain and simulation parameters.

Simulation parameters	Value
Particle diameter, d_p (μm)	75/150/300
Domain size, $L_0(d_p \times d_p \times d_p)$	$240 \times 240 \times 960$
Grid size, $(d_p \times d_p \times d_p)$	$3 \times 3 \times 3$
Acceleration due to gravity, $\|\mathbf{g}\|$ (m/s^2)	9.81/2.45
Domain-average solid volume fraction, $\langle\phi\rangle$ (m/s^2)	0.1/0.3
Number of particles	$10.5 \times 10^6/31.5 \times 10^6$
Particle density, ρ_p (kg/m^3)	1500
Real Young's modulus, Y^R (Pa)	7×10^{10}
Soft Young's modulus used in simulations, Y^S (Pa)	10^6
Poisson's ratio, ν	0.42
Restitution coefficient, e	0.9
Particle-particle friction coefficient, μ_p	0.5
Real Hamaker constant, A^R (J)	$10^{-19}/10^{-18}$
Minimum separation distance for real Young's modulus, $s^R_{\min}$ (m)	10^{-9}
Minimum separation distance for soft Young's modulus, $s^S_{\min}$ (m)	1.641×10^{-7}
Gas density, ρ_g (kg/m^3)	1.3
Gas viscosity, μ_g (Pa s)	1.8×10^{-5}
Characteristic quantities	**Value**
Stokes relaxation time, $\tau_p^{St} = \frac{\rho_p {d_p}^2}{18\mu_g}$ (s)	0.026 ($d_p = 75\ \mu$m)
	0.104 ($d_p = 150\ \mu$m)
	0.417 ($d_p = 300\ \mu$m)
Terminal velocity based on Wen and Yu[48] drag law, v_t (m/s)	0.219 ($d_p = 75\ \mu$m; $\|\mathbf{g}\| = 9.81$ m/s^2)
	0.649 ($d_p = 150\ \mu$m; $\|\mathbf{g}\| = 9.81$ m/s^2)
	1.533 ($d_p = 300\ \mu$m; $\|\mathbf{g}\| = 9.81$ m/s^2)
	0.0597 ($d_p = 75\ \mu$m; $\|\mathbf{g}\| = 2.45$ m/s^2)
Particle Froude number, $Fr_p = {v_t}^2/(\|\mathbf{g}\| d_p)$	65 ($d_p = 75\ \mu$m; $\|\mathbf{g}\| = 9.81$ m/s^2)
	286 ($d_p = 150\ \mu$m; $\|\mathbf{g}\| = 9.81$ m/s^2)
	799 ($d_p = 300\ \mu$m; $\|\mathbf{g}\| = 9.81$ m/s^2)
	19 ($d_p = 75\ \mu$m; $\|\mathbf{g}\| = 2.45$ m/s^2)
Particle Reynolds number, $Re_p = \frac{\rho_g v_t d_p}{\mu_g}$	1.18 ($d_p = 75\ \mu$m; $\|\mathbf{g}\| = 9.81$ m/s^2)
	7.03 ($d_p = 150\ \mu$m; $\|\mathbf{g}\| = 9.81$ m/s^2)
	33.23 ($d_p = 300\ \mu$m; $\|\mathbf{g}\| = 9.81$ m/s^2)
	0.32 ($d_p = 75\ \mu$m; $\|\mathbf{g}\| = 2.45$ m/s^2)
Particle Stokes number, $St_p = \frac{1}{18}\frac{\rho_p}{\rho_g} Re_p$	76 ($d_p = 75\ \mu$m; $\|\mathbf{g}\| = 9.81$ m/s^2)
	451 ($d_p = 150\ \mu$m; $\|\mathbf{g}\| = 9.81$ m/s^2)
	2130 ($d_p = 300\ \mu$m; $\|\mathbf{g}\| = 9.81$ m/s^2)
	20 ($d_p = 75\ \mu$m; $\|\mathbf{g}\| = 2.45$ m/s^2)
Particle Bond number, $Bo_p = F^{\max}_{\text{coh}}/(m_p\ \|\mathbf{g}\|)$ where $F^{\max}_{\text{coh}} = \frac{A^R d_p}{24 {s^R_{\min}}^2}$	96 ($d_p = 75\ \mu$m; $A^R = 10^{-19}$ J)
	960 ($d_p = 75\ \mu$m; $A^R = 10^{-18}$ J)

Two additional simulations with particle Bond numbers of 96 and 960 were performed.

We performed simulations in periodic domains in which one can examine the flow dynamics without wall-induced restrictions. To drive the flow in this periodic domain, we decompose the pressure term p_g in Eq. (A14) into two components as follows: $p_g(\boldsymbol{x}, t) = p_g''(\boldsymbol{x}, t) - \bar{\rho}|\boldsymbol{g}|(z - z_o)$. Here, p_g'' is the computed gas pressure that obeys the periodic boundary condition and $\bar{\rho}|\boldsymbol{g}|(z - z_o)$ represents the mean vertical pressure drop due to the total mass of a two-phase mixture; $\bar{\rho}$ is the domain-averaged mixture density; z is the coordinate in the direction that is opposite of gravity; and z_o is a reference elevation. The simulations were run for a sufficiently long duration ($10\ \tau_p^{St}$) to ensure that a statistical steady state is reached (see Table I for the definition of Stokes relaxation time, τ_p^{St}). Subsequently, snapshots were collected at every τ_p^{St} time instant for a duration of $20\ \tau_p^{St}$. Snapshots of the particle volume fraction fields obtained in simulations with different domain-averaged solid volume fractions are shown in Fig. 1 for particles with a diameter of 75 μm.

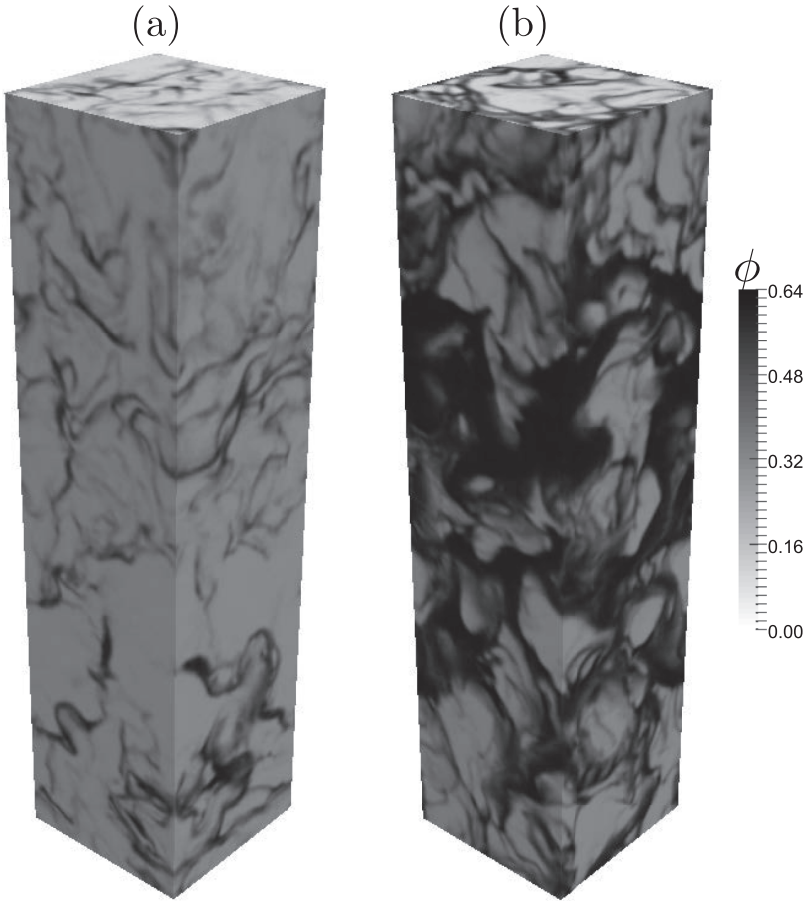

FIG. 1. Snapshots of the particle volume fraction field in a periodic domain. Simulation parameters are listed in Table I. Domain-averaged particle volume fraction $\langle\phi\rangle$: (a) 0.1 and (b) 0.3. The gray scale axis ranges from 0 (white) to 0.64 (black). The particle Froude number is 65.

III. FILTERING PROCEDURE AND SUB-GRID QUANTITIES

The correction to the drag force needed for Euler-Euler simulations with coarser fluid grids was deduced by filtering the results from Euler-Lagrange simulations. The macroscopic quantities were filtered using various filter sizes Δ_f around each computational node. The filtered solid volume fraction is computed by

$$\overline{\phi}(\mathbf{x},t) = \iiint \phi(\mathbf{r},t)G(\mathbf{r}-\mathbf{x})d\mathbf{r}, \tag{1}$$

where $G(\mathbf{r}-\mathbf{x})$ is a weight function which satisfies $\iiint G(\mathbf{r})d\mathbf{r} = 1$. The box filter kernel employed in all the results presented here is given by

$$G(\mathbf{r}-\mathbf{x}) = \begin{cases} \frac{1}{\Delta_f^3}, & \text{if } |\mathbf{r}-\mathbf{x}| \le \frac{\Delta_f}{2}, \\ 0, & \text{otherwise.} \end{cases} \tag{2}$$

Similarly, the filtered gas velocity is defined as

$$\tilde{u}_g(\mathbf{x},t) = \frac{1}{(1-\overline{\phi})} \iiint G(\mathbf{r}-\mathbf{x})(1-\phi(\mathbf{r},t))u_g(\mathbf{r},t)d\mathbf{r}. \tag{3}$$

For the particle phase, we first compute the Eulerian solid velocity $u_s(\mathbf{x}, t)$ by mapping the particle velocity $\boldsymbol{v}(\mathbf{x},t)$ to the cell centers in *a priori* manner by using the mollification kernel given in Eq. (A15). Then, we compute the filtered solid velocity by

$$\tilde{u}_s(\mathbf{x},t) = \frac{1}{\overline{\phi}} \iiint G(\mathbf{r}-\mathbf{x})\phi(\mathbf{r},t)u_s(\mathbf{r},t)d\mathbf{r} \tag{4}$$

and the filtered Eulerian drag coefficient as

$$\overline{\beta}_i = \frac{\overline{\beta\,(u_{g,i}-u_{s,i})}}{(\tilde{u}_{g,i}-\tilde{u}_{s,i})}, \tag{5}$$

where β is the "microscopic" Eulerian drag coefficient (namely, the Wen and Yu[48] drag law used in our simulations).

Igci *et al.*[19] introduced a term representing correlated fluctuations in the solid volume fraction and the gas pressure gradient into the filtered drag force. In this study, we do not consider this term in the filtered drag force.

A. Sub-grid drift velocity

Following the studies by Parmentier *et al.*[21] and Ozel *et al.*[14] and analogously in the framework of Reynolds-averaged kinetic theory by Fox[49] and Capecelatro *et al.*,[50,51] the filtered Eulerian drag force is written as

$$\overline{\beta(u_{g,i}-u_{s,i})} \approx \beta^*\,(\widetilde{u}_{g,i}-\widetilde{u}_{s,i}+\tilde{v}_{d,i}), \tag{6}$$

where β^* is the "microscopic" drag coefficient evaluated at the filtered particle volume fraction and the filtered phase velocities. In the studies of Parmentier *et al.*[21] and Ozel *et al.*,[14] β^* is defined as $\overline{\phi}\rho_p/\tilde{\tau}_p$, where $\tilde{\tau}_p$ is the "resolved" relaxation time (see Sec. 3.1 of Ozel *et al.*[14] for details). In Eq. (6), the sub-grid drift velocity $\tilde{v}_{d,i}$ is defined as

$$\overline{\phi}\tilde{v}_{d,i} = \overline{\phi\,(u_{g,i}-u_{s,i})} - \bar{\phi}\,(\tilde{u}_{g,i}-\tilde{u}_{s,i}) \tag{7}$$

or by using the definition [Eq. (4)]

$$\tilde{v}_{d,i} = \frac{\overline{\phi\,u_{g,i}}}{\overline{\phi}} - \tilde{u}_{g,i}. \tag{8}$$

In words, the sub-grid drift velocity is the difference between the filtered gas velocity and the filtered gas velocity seen by the particles. In a physical sense, the sub-grid drift velocity takes into account for inhomogeneities inside the filtering volume emerging as a local correlation between the solid volume fraction and gas velocity. The sub-grid drift velocity $\tilde{v}_{d,i}$ cannot be directly obtained from the coarse-grid simulations and needs a specific closure that will be discussed later.

B. Scalar variance of solid volume fraction

The sub-grid scalar variance of a conserved scalar is a key quantity for scalar mixing at the small scales of a turbulent flow and thus it is an important modeling parameter in large eddy simulations of turbulent reacting flows.[52–54] With an inspiration from single-phase turbulent reactive flow modeling, we attempt to model the sub-grid contribution of the drag term by using the sub-grid scalar variance of solid volume fraction. The sub-grid scalar variance of solid volume fraction $\overline{\phi'^2}(\mathbf{x}, t)$ is defined as follows:

$$\overline{\phi'^2}(\mathbf{x}, t) = \overline{(\phi(\mathbf{x}, t) - \overline{\phi}(\mathbf{x}, t))^2}. \tag{9}$$

For the sake of simplicity, we drop the spatial position $\mathbf{x}$ and time t and write it explicitly as follows:

$$\overline{\phi'^2} = \overline{\phi^2} - 2\,\overline{\phi}\overline{\phi} + \overline{\phi}^2. \tag{10}$$

It is worth noting that $\bar{\bar{\phi}} \neq \bar{\phi}$, which is not equivalent in the Reynolds averaging, is due to the property of the convolution kernel operator. However, the correlation between $\overline{\phi}$ and ϕ raises additional modeling issues for the practical applications. By following Jiménez *et al.*,[55] the scalar variance is defined as a statistical quantity which can be defined as follows:

$$\overline{\phi_*'^2} = \overline{\phi^2} - \overline{\phi}^2. \tag{11}$$

Herein, we use $\overline{\phi_*'^2}$ instead of $\overline{\phi'^2}$ for modeling.

IV. FILTERED DRAG RESULTS

In this section, we present statistical analyses of the filtered Eulerian drag coefficient as a function of the drift velocity and the scalar variance of solid volume fraction. As noted previously, the drift velocity and the scalar variance of solid volume fraction have already been used in the literature to infer the filtered drag coefficient.[14,21,24,49–51,56] The general approach to extract the filtered drag force and sub-grid quantities is as follows. We first gather the snapshots from simulation results, and a user-specified filter size is then employed to filter the drag force, phase velocities, and solid volume fraction. Subsequently, we compute the solid volume fraction-gas velocity correlation and then the drift velocity [Eq. (8)] and the scalar variance [Eq. (11)]. The filtered Eulerian drag coefficient data are then binned in terms of the filtered solid volume fraction, filter size, drift velocity, and scalar variance, and all the realizations in each bin are averaged to obtain mean results. Additionally, the effects of particle and domain sizes, domain-averaged volume fractions, gravitational accelerations, and cohesion levels on the filtered drag force are also investigated. We present the filtered Eulerian drag coefficient results in scaled form by dividing the "microscopic" drag coefficient evaluated at the filtered solid volume fraction and the filtered phase velocities. The drift velocity is scaled by the filtered relative velocity $\tilde{u}_{g,i} - \tilde{u}_{s,i}$ as well. Henceforth, we refer to the ratio of the filtered and the microscopic drag coefficients as the scaled drag coefficient and the ratio of the drift velocity and the filtered relative velocity as the scaled drift velocity.

A. Effect of filter size

The scaled drag coefficient as a function of the scaled drift velocity for various filter sizes at filtered solid volume fraction $\overline{\phi}$ equal to 0.1 is shown in Fig. 2(a). It reveals that the scaled drag coefficient increases linearly as the scaled drift velocity increases. However, as the scaled drift velocity approaches zero, the trend deviates from linearity and the scaled drag coefficient becomes larger than one. At first, this is surprising and it seems counter-intuitive. If the distribution of particles and the gas velocity inside the filter region is uniform, the drift velocity would be zero; for this state, one would expect the filtered drag ratio to be unity. This clearly comes across as a counter-example. Thus, the results in Fig. 2(a) readily reveal

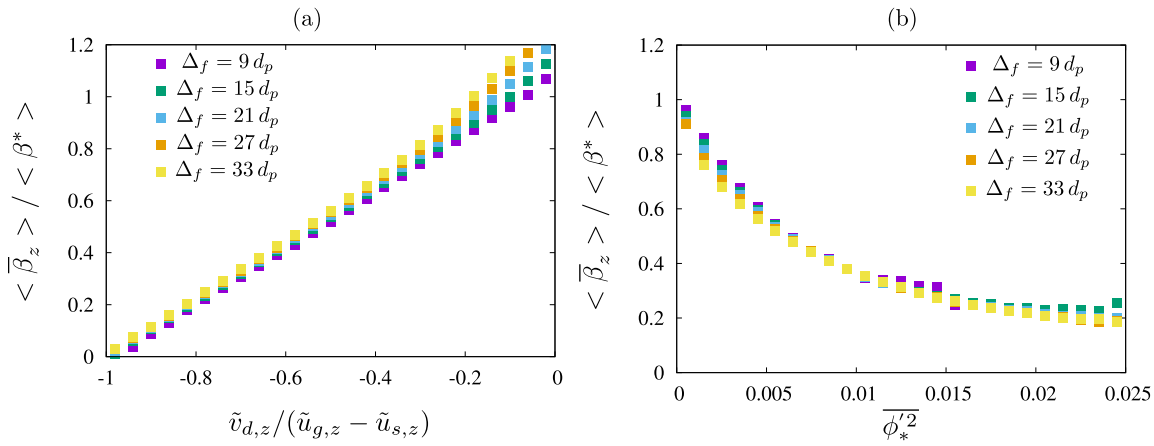

FIG. 2. Scaled filtered Eulerian drag coefficient as a function of (a) the scaled drift velocity and (b) the scalar variance of solid volume fraction for various filter sizes. The reference drag coefficient β^* is based on the filtered relative velocity and the filtered solid volume fraction. Domain-averaged solid volume fraction $\langle\phi\rangle = 0.1$; filtered volume fraction $\overline{\phi} = 0.1$; Froude number 65. Simulation parameters are summarized in Table I.

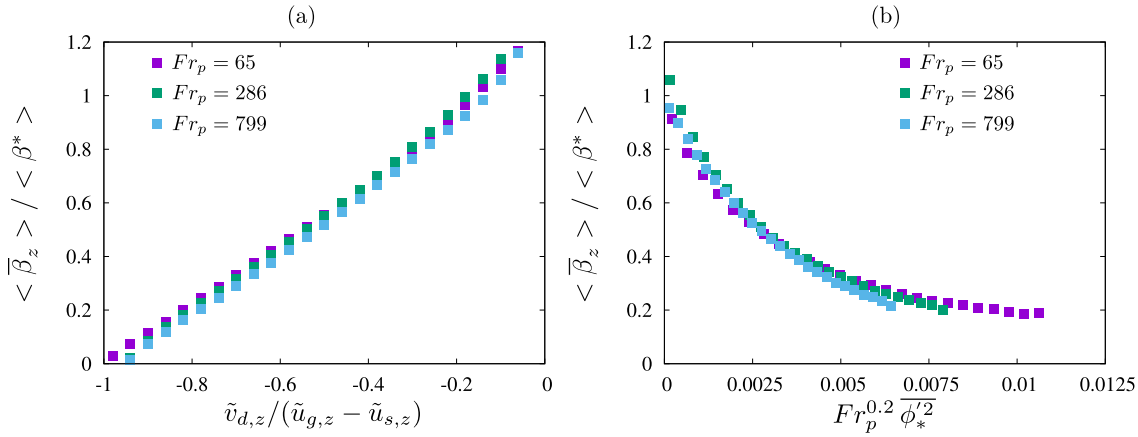

FIG. 3. Scaled filtered Eulerian drag coefficient as a function of (a) the scaled drift velocity and (b) the scalar variance of solid volume fraction for various particles sizes (Froude numbers 65, 286, and 799). The reference drag coefficient β^* is based on the filtered relative velocity and the filtered solid volume fraction. Domain-averaged solid volume fraction $\langle\phi\rangle = 0.1$; filtered volume fraction $\overline{\phi} = 0.1$; filter size $\Delta_f = 27\ d_p$. Simulation parameters are summarized in Table I.

that a second (perhaps weaker) marker would be needed to explain this anomalous result (more on this later).

The scaled drag coefficient as a function of the scalar variance of solid volume fraction for various filter sizes at $\overline{\phi} = 0.1$ is shown in Fig. 2(b). It shows that the scaled drag coefficient decreases as the scalar variance increases. The scalar variance is one measure of the level of inhomogeneities; larger inhomogeneities lead to larger scalar variance values which, in turn, signal a higher drag correction. One can see from Figs. 2(a) and 2(b) that the scaled drag coefficient is essentially independent of the filter size for both sub-grid quantities.

B. Effect of particle size

Figures 3(a) and 3(b) present the scaled drag coefficient as a function of the scaled drift velocity and the scalar variance of solid volume fraction for two other particle sizes (equivalently, particle Froude numbers) at $\overline{\phi} = 0.1$. The scaled drift velocity dependency of the scaled drag coefficient is identical for different particle sizes. However, for the scalar variance dependency, an additional scaling, $Fr_p^{0.2}$, is needed to collapse the scaled drag coefficients for different particle sizes. This figure suggests that the drift velocity is a better marker than the scalar variance of solid volume fraction.

C. Effect of domain size

Capecelatro *et al.*[57] performed highly resolved Euler-Lagrangian simulations of dilute gas-solid flows ($\langle\phi\rangle = 0.01$) in a fully periodic prism with various sizes to probe the effect of the domain-size on the particle cluster size and phase velocity fluctuations. They found that the cluster size and the particle phase kinetic energy increase as the domain size increases. However, the upper limit of the particle cluster size or the scaling of the cluster size with respect to the domain size is still not known. We performed simulations with two additional domain sizes: half and quarter of the reference domain L_0 (see Table I), to study the effect of the domain size on the filtered drag force. The scaled drag coefficient as a function of the scaled drift velocity and the scalar variance of solid volume fraction for various domain sizes are shown in Figs. 4(a) and 4(b), respectively. One can see that there is no significant difference of the scaled drag coefficient for different domain sizes.

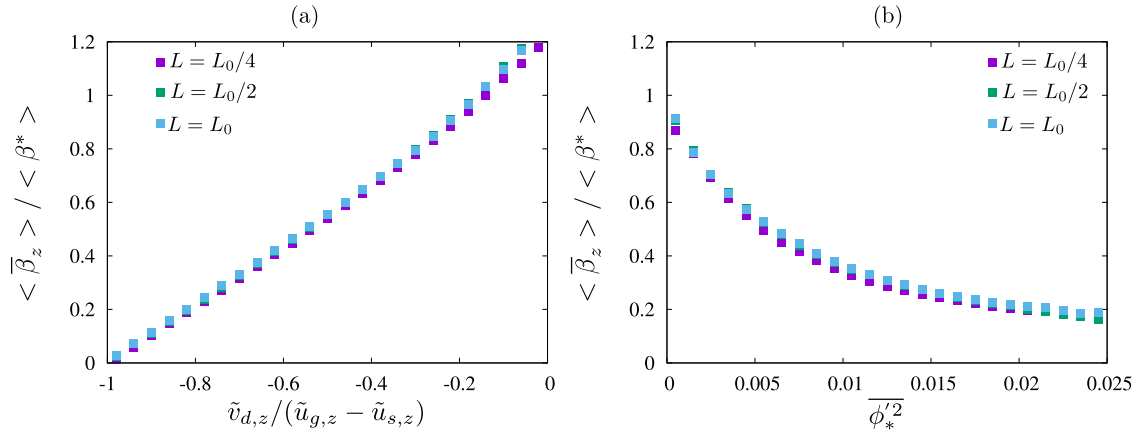

FIG. 4. Scaled filtered Eulerian drag coefficient as a function of (a) the scaled drift velocity and (b) the scalar variance of solid volume fraction for various domain sizes. The reference drag coefficient β^* is based on the filtered relative velocity and the filtered solid volume fraction. Domain-averaged solid volume fraction $\langle\phi\rangle = 0.1$; filtered volume fraction $\overline{\phi} = 0.1$; Froude number 65; Filter size 27 d_p. Simulation parameters are summarized in Table I.

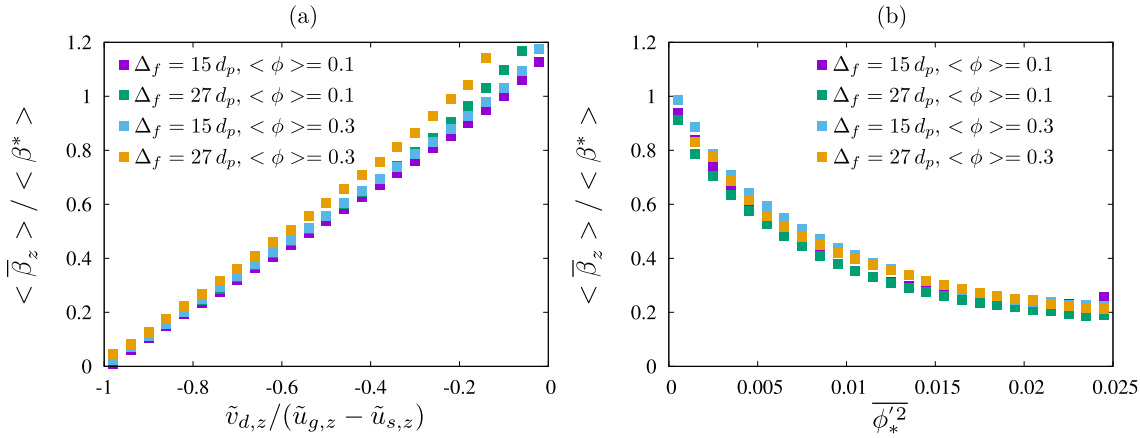

FIG. 5. Scaled filtered Eulerian drag coefficient as a function of (a) the scaled drift velocity and (b) the scalar variance of solid volume fraction for two domain-averaged solid volume fractions. The reference drag coefficient β^* is based on the filtered relative velocity and the filtered solid volume fraction. Filtered volume fraction $\overline{\phi} = 0.1$; Froude number 65; filter sizes Δ_f = 15 and 27 d_p; Simulation parameters are summarized in Table I.

D. Effect of domain-averaged solid volume fraction

Depending on the domain-averaged solid volume fraction, one can get different flow regimes: clusters and streamers in dilute and moderately dilute flows and voids in dense flows. We present the effect of the domain-averaged solid volume fraction on the scaled drag coefficient as a function of the scaled drift velocity in Fig. 5(a) and as a function of the scalar variance of solid volume fraction in Fig. 5(b). The filtered results nearly collapse for different domain-averaged solid volume fractions and filter sizes. Slight differences remain, which indicate that further improvement could be achieved with an additional marker, as discussed later.

E. Effect of gravitational acceleration

To study the effect of gravity on drag force, an additional simulation was performed with one quarter of the reference gravity. With a smaller gravitational acceleration, the Froude number is smaller; and as the relative velocity is smaller, the particle Reynolds number is smaller as well (see Table I for Froude and Reynolds numbers corresponding to different gravitational accelerations). In other words, this simulation allows us to study the effect of Reynolds and Froude numbers on the filtered drag coefficient. Figures 6(a) and 6(b) show the effect of gravitational acceleration on the dependence of the scaled drag coefficient on the scaled drift velocity and the scalar variance of solid volume fraction for two filter sizes. The scaled drag coefficients versus the drift velocity for different gravitational accelerations are nearly identical, but there is a somewhat larger difference in the scalar variance dependency of the scaled drag coefficients. In addition to the parametric study presented in the main text, we also show the scaled drag coefficient as a function of the scaled drift velocity with different filter types (box and Gaussian filters) and drag laws[48,58] for $\Delta_f = 27\,d_p$ and $\langle\phi\rangle = 0.1$ in Appendix B. Results show that the dependency of the scaled filtered drag on the scaled drift velocity is independent of the choice of the microscopic drag law, and the departure from linear relationship of the scaled filtered drag and the scaled drift velocity is less significant with a Gaussian filter.

F. Effect of filtered solid volume fraction

In Secs. IV A–IV E, we presented the scaled drag coefficient versus the scaled drift velocity and the scalar variance of

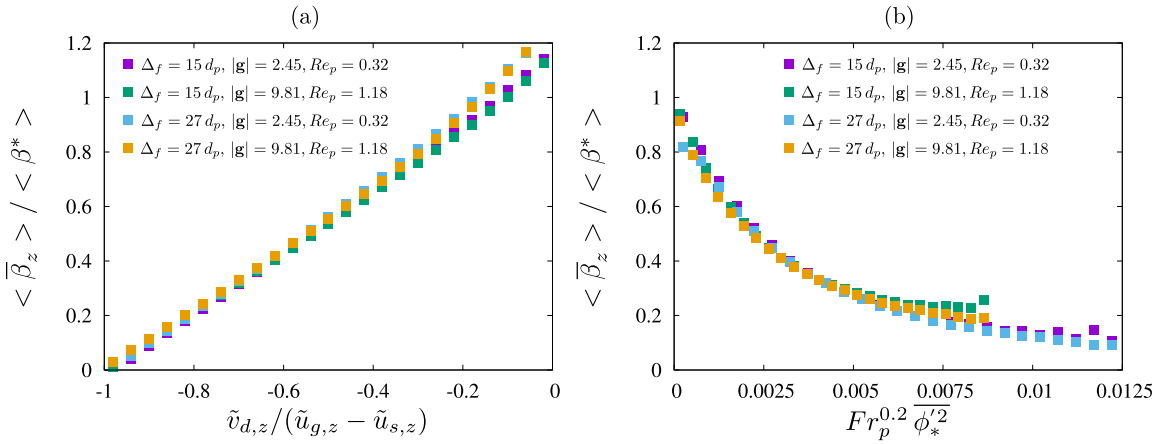

FIG. 6. Scaled filtered Eulerian drag coefficient as a function of (a) the scaled drift velocity and (b) the scalar variance of solid volume fraction for other gravity accelerations. The reference drag coefficient β^* is based on the filtered relative velocity and the filtered solid volume fraction. Domain-averaged solid volume fraction $\langle\phi\rangle = 0.1$; filtered volume fraction $\overline{\phi} = 0.1$; Froude numbers 19 and 65; filter sizes Δ_f = 15 and 27 d_p. Simulation parameters are summarized in Table I.

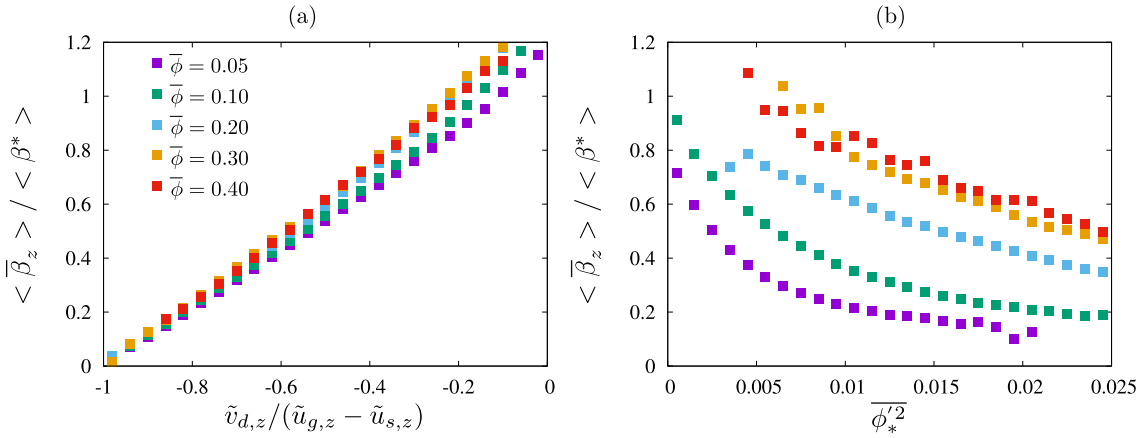

FIG. 7. Scaled filtered Eulerian drag coefficient as a function of (a) the scaled drift velocity and (b) the scalar variance of solid volume fraction for various filtered solid volume fractions. The reference drag coefficient β^* is based on the filtered relative velocity and the filtered solid volume fraction. Domain-averaged solid volume fraction $\langle\phi\rangle = 0.1$; Froude number 65; filter size 27 d_p. Simulation parameters are summarized in Table I.

solid volume fraction for various particle and domain sizes, gravitational accelerations, and domain-averaged solid volume fractions at one specific filtered solid volume fraction $\overline{\phi} = 0.1$. Here, we show how the scaled drift velocity and the scalar variance dependency of the scaled drag coefficient varies with the filtered solid volume fraction. Figure 7(a) shows the scaled drag coefficient versus the scaled drift velocity for various filtered solid volume fractions. It is nearly independent of

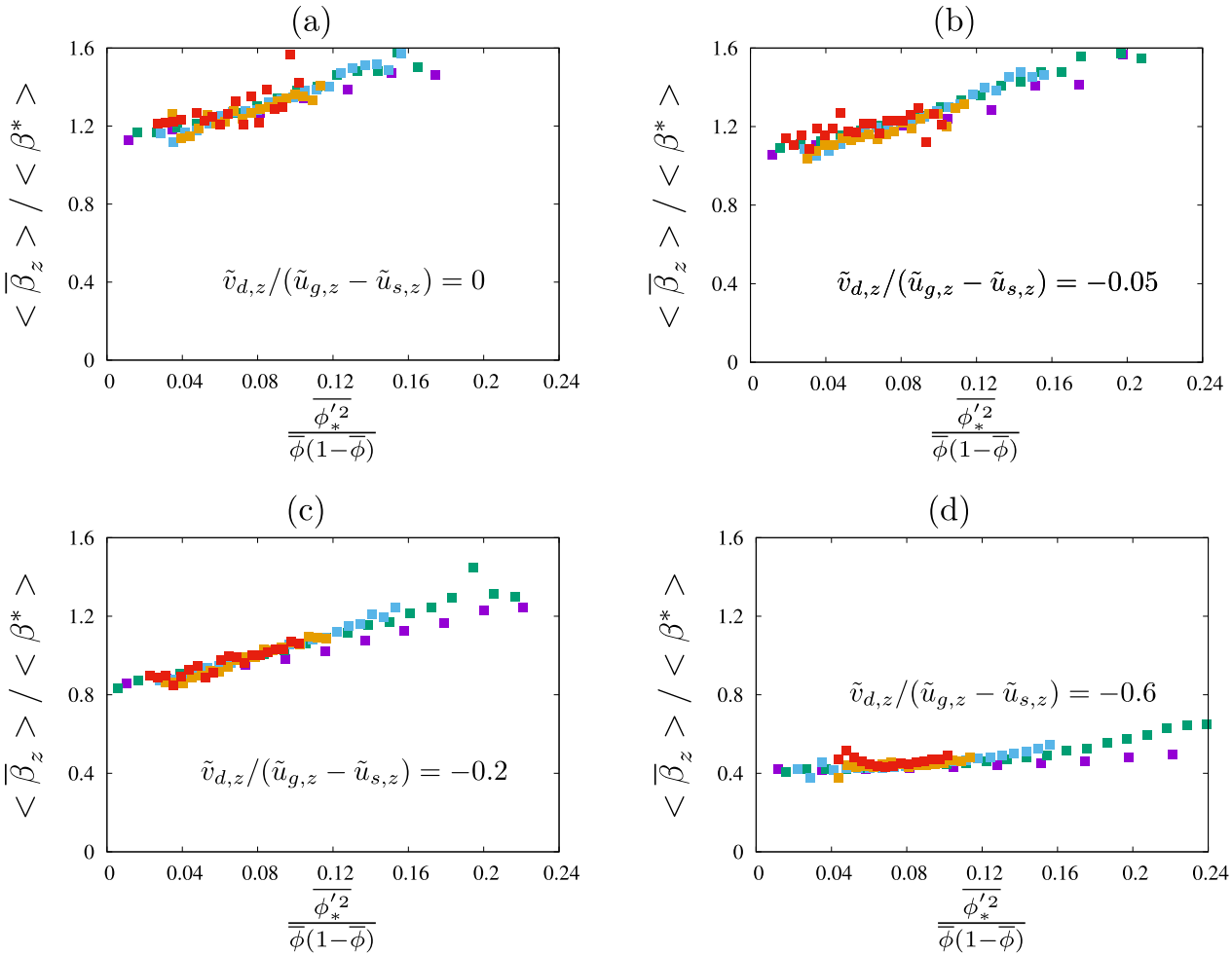

FIG. 8. Scaled filtered Eulerian drag coefficient as a function of the scalar variance of solid volume fraction for various filtered solid volumes at specific scaled drift velocities. Scaled drift velocities $\tilde{v}_{d,z}/(\tilde{u}_{g,z} - \tilde{u}_{s,z})$ are (a) 0, (b) −0.05, (c) −0.2, and (d) −0.6. The legend is the same as in Fig. 7. The reference drag coefficient β^* is based on the filtered relative velocity and the filtered solid volume fraction. Domain-averaged solid volume fraction $\langle\phi\rangle = 0.1$; Froude number 65; filter size 27 d_p. Simulation parameters are summarized in Table I.

the filtered solid volume fraction, and once again, the scaled drag coefficient increases linearly as the scaled drift velocity increases except for large values of drift velocity. In Fig. 7(b), the scaled drag coefficient is shown as a function of the scalar variance for various solid volume fractions. One can see that the scaled drag coefficient is not just a function of the scalar variance alone.

We now turn our attention to the spread that we see in the plots displaying the scaled drag coefficient versus the scaled drift velocity. Figure 8 shows the scaled drag coefficient as a function of the scalar variance of solid volume fraction for various filtered solid volume fractions at specific scaled drift velocities. One can see that the scalar variance could be used as a second marker for the drift velocity modeling. In particular, for $\tilde{v}_{d,z}/(\tilde{u}_{g,z} - \tilde{u}_{s,z}) > -0.1$, including scalar variance into the model will provide improvement. Following that analysis, we rescaled the abscissa in Fig. 7(b) by $\overline{\phi}(1-\overline{\phi})$ to bring the datasets together, but non-negligible $\overline{\phi}$ dependence still remains (not shown). Introducing the scalar variance into the scaled drag coefficient modeling will be discussed in Sec. V.

G. Effect of cohesion

It is well-known that cohesive force may lead to agglomeration of particles and affect fluidization behavior of particles.[27,28,30,31,59–61] In particular, the micro-structure of particles is significantly affected by cohesive force, and as a consequence, the drag force is expected to be different from the non-cohesive case. We performed two additional simulations with low and high cohesion levels to probe the importance of particle cohesion on the extent of correction to the drag force. In these simulations, the Hamaker constants for low and high cohesion levels are $A^R = 10^{-19}$ and 10^{-18} J, respectively, and the domain-averaged solid fraction $\langle\phi\rangle$ is equal to 0.3. In terms of dimensionless quantities, we express the strength of cohesion in terms of the particle Bond number (see Table I). For the low and high cohesion cases, the particle Bond number assumes values of 96 and 960, respectively. The number of contacts per particles for simulations with and without cohesive force is given in Table II. The number of contacts increases as the cohesion force increases and the micro-structure of particles are significantly altered by cohesion. Similar to the non-cohesive case, we computed the filtered drag coefficient and binned the drift velocity and the scalar variance of solid volume fraction. The scaled drag coefficient results versus the scaled drift velocity and the scalar variance are shown Figs. 9(a) and 9(b). The scaled drag coefficient results with respect to the scaled drift velocity collapse for different cohesion levels. However, the effect of cohesion emerges weakly in the scalar variance results.

TABLE II. Number of contacts per particle for the simulations with Hamaker constants A^R of 0 (reference case), 10^{-19}, and 10^{-18} J.

Hamaker constant, A^R (J)	Number of contacts
0	0.699
10^{-19}	0.998
10^{-18}	2.955

It is shown that the dependency of the scaled drag coefficient on the scaled drift velocity is the same for non-cohesive and cohesive particles. However, cohesive particles can be expected to form aggregates, which would fluidize differently than the primary particles. This would lead to different drift velocity values. A common and powerful approach to modeling gas-particle flows where dynamic agglomerates form through particle-particle cohesion has been to couple Eulerian continuity and momentum balances with a population balance model.[62–64] In slightly cohesive systems where particle aggregates survive only fleetingly, for example, in weakly cohesive Geldart group A particles subjected to fluidization, a simpler approach that incorporates the effects of cohesion into the drag and stress models directly (and not require additional population balance) is attractive. For example, studies have sought to extend the kinetic theory of granular materials, commonly used to simulate fluidization[6] to cohesive particles.[65–67] In this approach, cohesion would explicitly enter in the Euler-Euler equations through particle phase stresses; it is then reasonable

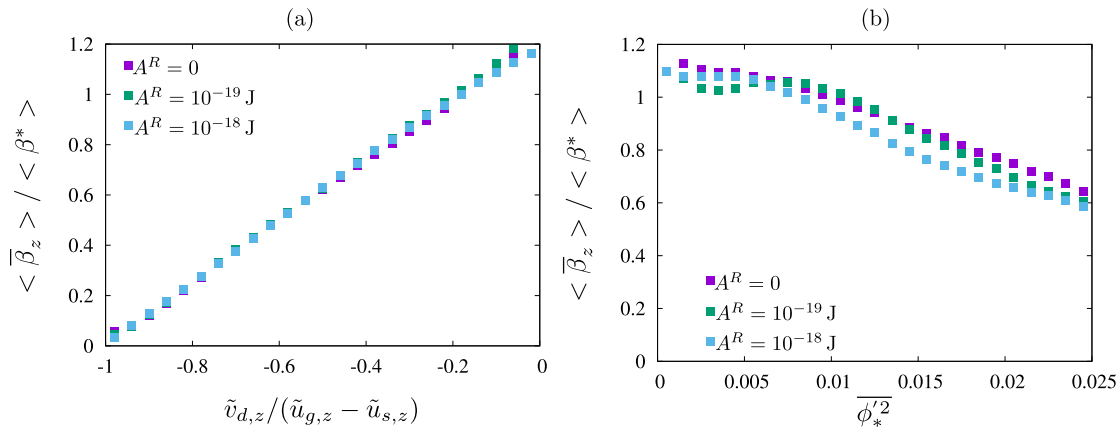

FIG. 9. Scaled filtered Eulerian drag coefficient as a function of (a) the scaled drift velocity and (b) the scalar variance of solid volume fraction for two cohesiveness levels: $A^R = 10^{-19}$ and 10^{-18} J. The reference drag coefficient β^* is based on the filtered relative velocity and the filtered solid volume fraction. Domain-averaged solid volume fraction $\langle\phi\rangle = 0.3$; filtered volume fraction $\overline{\phi} = 0.4$; Froude number 65; filter size 27 d_p. Simulation parameters are summarized in Table I.

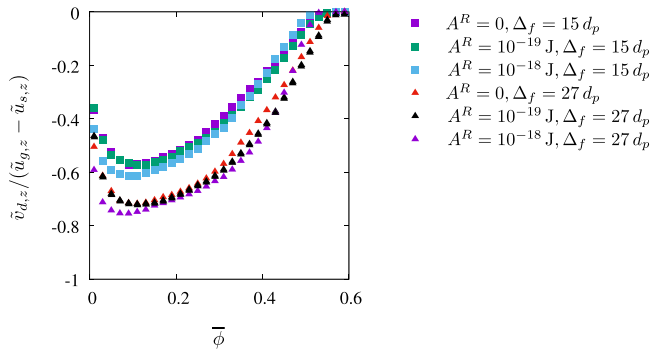

FIG. 10. Scaled drift velocity as a function of the filtered solid volume fraction for the non-cohesive case and two cohesiveness levels: $A^R = 10^{-19}$ and 10^{-18} J. Filter sizes are $\Delta_f = 15\,d_p$ and $27\,d_p$. Domain-averaged solid volume fraction $\langle\phi\rangle = 0.3$; Froude number 65. Simulation parameters are summarized in Table I.

to anticipate that cohesion would enter in the filtered Euler-Euler models through the stress terms as well. The present study has not addressed stress modeling but focuses only on the drag force model.

We find that a correction for cohesion is not needed for the model relating the scaled drag coefficient to the scaled drift velocity. It then raises a question as to whether a model to estimate the drift velocity in filtered model simulations should explicitly account for the effect of cohesion.

The Hamaker constant for the "high cohesion" case considered in this study is larger than that of most common materials. Even at such high cohesion levels, there seems to be only a weak change in the scaled drift velocity characteristics, as illustrated in Fig. 10, where we have plotted the scaled drift velocity against the filtered solid volume fraction for two different filter sizes and two different cohesion levels. It is clear that cohesion changes the results minimally, with its effect being much weaker than that of the filter size. Thus, it appears that in filtered models for flows of mildly cohesive Geldart group A particles, one can, as a reasonable first approximation, ignore the effect of cohesion on the constitutive model for the scaled drift velocity and let the effect of cohesion enter only through the stress model.

V. ASSESSMENTS OF MODELS FOR FILTERED DRAG COEFFICIENT IN TERMS OF SUB-GRID QUANTITIES

In order to estimate the scaled drag coefficient in filtered model simulations, we need (a) a model for it in terms of one or more sub-grid markers and (b) means of estimating these markers. In Secs. III and IV, we were concerned with the first of these two items. Here we will address the second. Before doing that we present computational data-derived models for the scaled drag coefficient in terms of the markers.

It is clear from Fig. 7(b) that a model for the scaled drag coefficient is not just a function of the scalar variance. At the very least, it must involve the filtered solid volume fraction, $\langle\overline{\beta}_z\rangle/\langle\beta^*\rangle = f(\overline{\phi}, \overline{\phi_*'^2})$. Strictly speaking, such a representation is applicable only for a specific set of values for the dimensionless groups, and so it is not satisfactory. Therefore, we will not discuss the form of this equation further. Nevertheless, we present below a representative example (non-cohesive particles with $Fr_p = 65$) to obtain a quantitative assessment of the model that uses only the scalar variance as a marker. Specifically, we used a genetic algorithm in conjunction with the data in Fig. 7(b) to create a look-up table.

In contrast, a model for the scaled drag coefficient in terms of the drift velocity is simpler and applicable to all values of dimensionless groups. It is given by

$$\frac{\langle\overline{\beta}_z\rangle}{\langle\beta^*\rangle} = 1 + \frac{\tilde{v}_{d,z}}{\tilde{u}_{g,z} - \tilde{u}_{s,z}}. \tag{12}$$

The results in Fig. 8 suggest that one can get a somewhat better prediction of the scaled drag coefficient by treating the scaled drift velocity and the scalar variance of solid volume fraction as two separate markers. Analysis of computational data from our simulations for various particle sizes, domain-average volume fractions, gravitational accelerations, and strengths of cohesion leads to a model of the form

$$\frac{\langle\overline{\beta}_z\rangle}{\langle\beta^*\rangle} = \left(1 + \frac{\tilde{v}_{d,z}}{\tilde{u}_{g,z} - \tilde{u}_{s,z}}\right)\left(1 + C^* \frac{\overline{\phi_*'^2}}{\overline{\phi}(1-\overline{\phi})}\right) \tag{13}$$

with the model constant C^* being 2.25 ± 0.5; the single marker model in terms of the scaled drift velocity [Eq. (12)] is obtained by neglecting the third term on the right-hand-side of Eq. (13). According to Eq. (13), if both the scaled drift velocity and scalar variance of volume fraction are zero, the scaled drag coefficient is unity. This removes the apparent anomaly discussed earlier in Sec. IV A. We then ask how good these correlations are by *a priori* analysis of data obtained in our computations. Although such an analysis was done for several different cases, we only present the results for one representative example involving non-cohesive particles with $Fr_p = 65$. It is worth noting that analysis of the other cases leads to a similar conclusion.

The drift velocity and the scalar variance are statistical sub-grid quantities computed by performing conditional averaging and they do have a scatter. Therefore, as an initial *a priori* test, we first assess their predictabilities for the effective drag modeling by computing the Pearson correlation coefficient and the probability density function of the relative error between exact filtered drag coefficients from simulation data and predicted filtered drag coefficients by using the drift velocity and the scalar variance. The Pearson correlation coefficient is defined as

$$r(x;y) = \frac{\sum_{i=1}^{n}(x_i - \bar{x})(y_i - \bar{y})}{\sqrt{\sum_{i=1}^{n}(x_i - \bar{x})^2}\sqrt{\sum_{i=1}^{n}(y_i - \bar{y})^2}} \tag{14}$$

with two datasets $(x_1, \ldots, x_n)$ and $(y_1, \ldots, y_n)$ each containing n values. The symbols $\bar{x}$ and $\bar{y}$ are the mean values of the datasets. The correlation coefficient $r(x;y)$, computed by Eq. (14), shows *a priori* predictability of basic model assumptions by quantifying the degree to which the structure of the filtered drag coefficient is captured by the model. To quantify the statistical accuracy of the models, we define the relative error as

$$e_i(x;y) \equiv \frac{x_i - y_i}{y_i}. \tag{15}$$

Pearson correlation coefficients between computed and predicted drag coefficients by using the drift velocity [Eq. (12)],

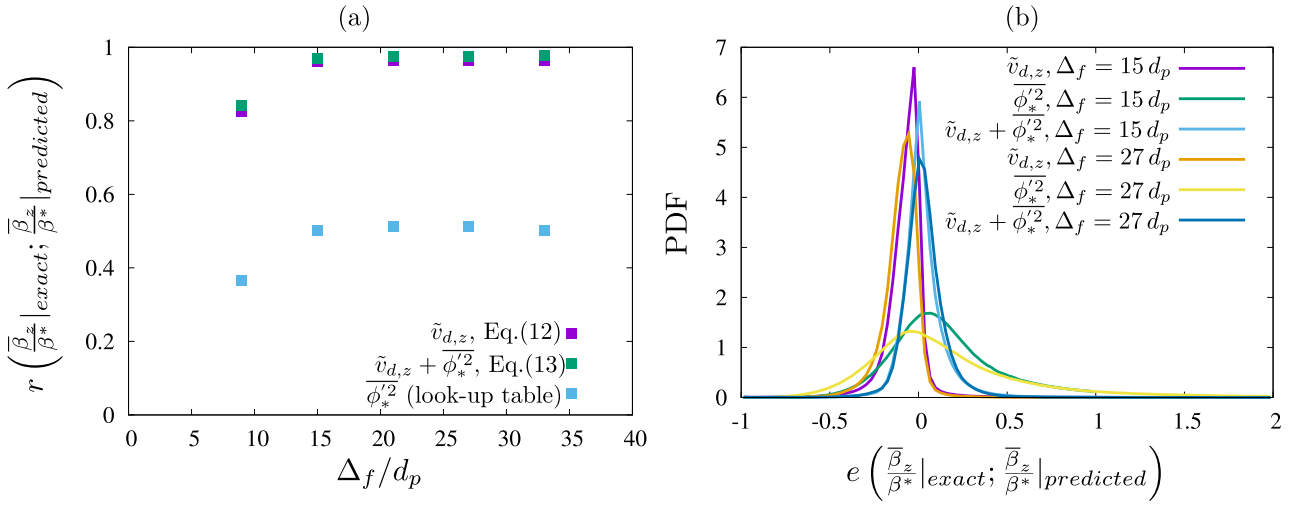

FIG. 11. (a) Pearson correlation coefficients between exact and predicted drag coefficients using the drift velocity [Eq. (12)], only the scalar variance (look-up table of $f(\phi, \overline{\phi_*'^2})$), and both drift velocity and scalar variance [Eq. (13)] for various filter sizes. (b) Probability distribution function of the relative error between exact and predicted drag coefficients using the drift velocity, only the scalar variance, and both the drift velocity and scalar variance for various filter sizes Δ_f = 15 d_p and 27 d_p. The reference drag coefficient β^* is based on the filtered relative velocity and the filtered solid volume fraction. Domain-averaged solid volume fraction $\langle\phi\rangle$ = 0.1; Froude number 65. Simulation parameters are summarized in Table I.

only the scalar variance (look-up table of $f(\phi, \overline{\phi_*'^2})$), and both drift velocity and scalar variance [Eq. (13)] are shown in Fig. 11(a). The drift velocity shows an excellent performance in terms of the correlation coefficient and it asymptotically reaches to the value of 0.95 as the filter size increases. Including the scalar variance of solid volume fraction into the drift model, Eq. (13) (green points), provides only a marginal improvement of the prediction. The correlation coefficient is around 0.6 when only the scalar variance of particle volume fraction is used as a marker. In view of this, we discard the scalar variance of solid volume fraction as a useful single marker and focus on the drift velocity as the most valuable single marker.

Figure 11(b) shows the probability distribution function (PDF) of the relative error between measured and predicted drag coefficients by using the drift velocity or the scalar variance of solid volume fraction for filter sizes of 15 d_p and 27 d_p. It is clear that the PDFs of relative error are significantly narrower when the drift velocity is used as the marker instead of the scalar variance. Using both the drift velocity and scalar variance of solid volume fraction leads to a small shift of the PDF towards positive abscissa values. The above correlation coefficient and PDF analyses assumed that we knew the value of drift velocity and the scalar variance of solid volume fraction, but one does not have direct access to them in filtered model simulations; they have to be estimated and the associated error can be expected to degrade the predictability of scaled drag coefficients. We now examine this issue for a model for the scaled drag coefficient relying only the scaled drift velocity. Parmentier *et al.*[21] and Ozel *et al.*[14] modeled the drift velocity as

$$\tilde{v}_{d,i} = \kappa\, h(\overline{\phi}) f(\Delta^*)\,(\tilde{u}_{g,i} - \tilde{u}_{s,i}), \tag{16}$$

where the constant κ is dynamically evaluated by a scale-similarity method. The local model constant κ could be positive or negative due to the local structure of the flow. Positive κ refers to the reduction of the drag force and the negative κ refers to the increase in the drag force.[68–70] We showed in an earlier study[36] that the function $h(\overline{\phi})$ computed from Euler-Lagrange simulations is of the form suggested by Parmentier *et al.*,[21]

$$h(\overline{\phi}) = -\sqrt{\frac{\overline{\phi}}{\phi_{\max}}}\left(1-\frac{\overline{\phi}}{\phi_{\max}}\right)^2 \times\left(1 - C_{h,2}\frac{\overline{\phi}}{\phi_{\max}} + C_{h,3}\left(\frac{\overline{\phi}}{\phi_{\max}}\right)^2\right) \tag{17}$$

with constants $C_{h,1}$, $C_{h,2}$, and $C_{h,3}$ assuming values of 0.1, 1.88, and 5.16 for non-cohesive particles with Fr_p = 65, respectively. The numerical values of the constants in this equation change somewhat for other Froude numbers, but this change is not relevant for the current model assessment analysis. The following model is proposed by Ozel *et al.*[14] to capture the filter size dependency,

$$f(\Delta^*) = \frac{\overline{\Delta}^{*2}}{C_{f,1} + \overline{\Delta}^{*2}} \tag{18}$$

with the constant $C_{f,1}$ equal to 0.15 and Δ^* is given by

$$\Delta^* = \frac{\overline{\Delta}}{\tilde{\tau}_p\,|\tilde{\mathbf{V}}_r|}, \tag{19}$$

where $\tilde{\tau}_p$ is the filtered relaxation time, $|\tilde{\mathbf{V}}_r|$ is the magnitude of the filtered relative velocity, and $\overline{\Delta}$ is the filter width. Our results extracted from Euler-Lagrange simulations for non-cohesive particles with Fr_p = 65 could be captured by

$$f(\Delta^*) = \frac{(\Delta/d_p)^2}{108 + (\Delta/d_p)^2}. \tag{20}$$

Note that in this equation, the filter size is scaled with d_p, which is different from the scaling relation used by Ozel *et al.*[14] This difference is irrelevant for the current analysis, as the analysis of predictability is being presented for a specific example. Using Eqs. (16), (17), and (20), along with the scale-similarity approach to estimate κ (see Refs. 21 and 14 for details), one

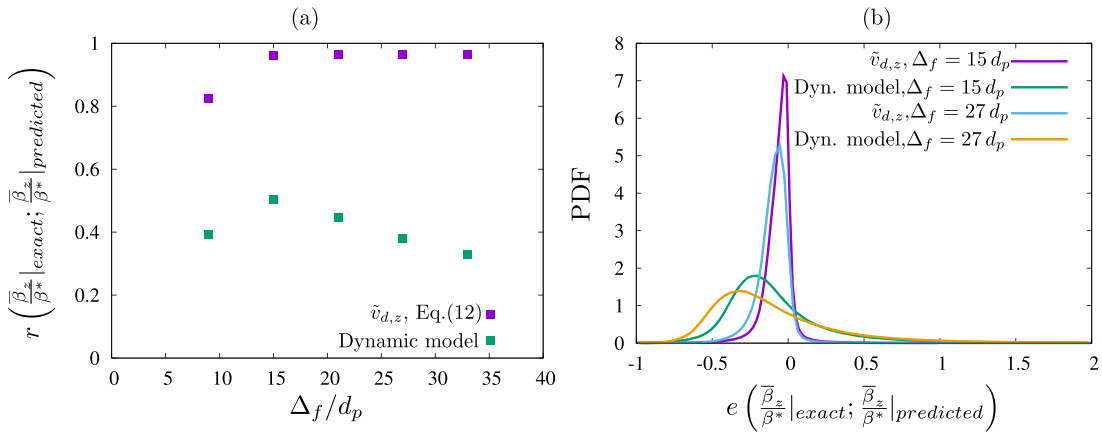

FIG. 12. (a) Pearson correlation coefficients between exact and predicted drag coefficients using the drift velocity, Eq. (12), and the dynamic drift velocity model, Eq. (16), for various filter sizes. (b) Probability distribution function of the relative error between exact and predicted drag coefficients using the drift velocity and the dynamic drift velocity model for filter sizes $\Delta_f = 15\,d_p$ and $27\,d_p$. The reference drag coefficient β^* is based on the filtered relative velocity and the filtered solid volume fraction. Domain-averaged solid volume fraction $\langle\phi\rangle = 0.1$; Froude number 65. Simulation parameters are summarized in Table I.

can first estimate the drift velocity from the filtered variables and then the scaled drag coefficient. The accuracy of this estimate can be judged through a Pearson correlation analysis. As shown in Fig. 12(a), the coefficient is now diminished, reflecting the error introduced by the scale-similarity model for the drift velocity. The corresponding PDF results are presented in Fig. 12(b).

It should be noted that several authors have sought to model the scaled drag coefficient using only quantities that would be readily available in filtered model simulations. As an example, we proposed a model for the scaled drag coefficient as a function of the filtered solid volume fraction and the filtered relative velocity. As discussed in Appendix C, such models are less satisfactorily.

VI. SUMMARY

We have performed Euler-Lagrange simulations of gas-solid flows in periodic domains to study the effective drag force model to be used in coarse-grained Euler-Lagrange and filtered Euler-Euler models. In these simulations, we varied particle and domain sizes, gravitational accelerations, domain-averaged solid volume fractions, and strengths of the van der Waals force by adjusting the Hamaker constant. We first applied the box filter on the simulation results and then computed the scaled Eulerian drag coefficient (drag coefficient normalized by the microscopic drag coefficient evaluated at the filtered solid volume fraction and filtered phase velocities) and the scaled drift velocity (drift velocity normalized by the filtered relative velocity) and scalar variance of solid volume fraction. The results show that the scaled drag coefficient is a simple function of the scaled drift velocity and it linearly decreases as the scaled drift velocity decreases. The findings in the current Euler-Lagrange simulations are consistent with what have been found in a lattice-Boltzmann-discrete-element-method study[71] for much smaller systems. The Euler-Euler simulations by Parmentier *et al.*[21] and Ozel *et al.*[14] considered much larger systems than the ones probed in our study, which also yielded similar results.

In contrast, the scaled drag coefficient is not a simple function of the scalar variance of solid volume fraction, making it a less attractive marker. However, it affords a modest improvement as a second marker, with the scaled drift velocity as the first marker. Interestingly, we found a little difference in the dependence of the scaled drag coefficient on the scaled drift velocity between cohesive and non-cohesive particles. Furthermore, the dependency of the drift velocity on the filtered volume fraction and filter size was unaffected by the strength of cohesion over a wide range. This led us to conclude that in the filtered Euler-Euler model for Geldart group A particles, one need not be concerned with the effect of cohesion on the drag closure. Differentiation between cohesive and non-cohesive systems is then expected to come from solid stress modeling.

We have also compared exact filtered drag coefficients observed in the simulations with those determined through a model using the drift velocity and the scalar variance extracted from simulations as single markers. We present Pearson correlation coefficients and probability density functions of relative error of exact and predicted drag coefficients and show that the drift velocity is a distinctly superior marker. The correlation coefficient is higher even for larger filter sizes, which is attractive from the point of view of coarse modeling. Using the scalar variance of solid volume fraction as a second marker, with the drift velocity being the first marker, it is shown to lead to a small improvement in the estimation of drag correction.

The sub-grid markers are not available in coarse-grid simulations and must be estimated to accurately predict the drag force. We assess the scale similarity model for drift velocity proposed by Parmentier *et al.*[21] and Ozel *et al.*[14] and find that the correlation coefficient is degraded appreciably. This suggests that we need a better model to estimate the drift velocity. A natural next step would be to develop a transport equation for the drift velocity, which is suggested as a direction for future study.

ACKNOWLEDGMENTS

This study was supported by ExxonMobil Research & Engineering Company.

APPENDIX A: MATHEMATICAL MODELING

In the Discrete Element Method,[42] particles are tracked by solving Newton's equations of motion,

$$m_i \frac{d\boldsymbol{v}_i}{dt} = \sum_j (\boldsymbol{f}^n_{c,ij} + \boldsymbol{f}^t_{c,ij}) + \sum_k \mathbf{f}_{v,ik} + \boldsymbol{f}_{g\to p,i} + m_i \boldsymbol{g}, \quad \text{(A1)}$$

$$I_i \frac{d\boldsymbol{\omega}_i}{dt} = \sum_j \boldsymbol{T}_{t,ij}. \quad \text{(A2)}$$

In the equations, particle i is spherical and has mass m_i, moment of inertia I_i, translational and angular velocities $\boldsymbol{v}_i$ and $\boldsymbol{\omega}_i$. $\boldsymbol{f}^n_{c,ij}$ and $\boldsymbol{f}^t_{c,ij}$ are the normal and tangential contact forces between two particles i and j; $\mathbf{f}_{v,ik}$ is the van der Waals force from the interaction between two particles i and k; $\boldsymbol{f}_{g\to p,i}$ is the total interaction force on the particle i due to surrounding gas (explained further below), and $m_i\boldsymbol{g}$ is the gravitational force. The torque acting on particle i due to particle j is $\boldsymbol{T}_{t,ij}$. $\boldsymbol{T}_{t,ij} = \boldsymbol{R}_{ij} \times \boldsymbol{f}^t_{c,ij}$, where $\boldsymbol{R}_{ij}$ is the vector from the center of particle i to the contact point. The particle contact forces $\boldsymbol{f}^n_{c,ij}$ and $\boldsymbol{f}^t_{c,ij}$ are calculated by following Refs. 72 and 73 as

$$\boldsymbol{f}^n_{c,ij} = \frac{4}{3} Y^* \sqrt{r^*} \delta_n^{3/2} \boldsymbol{n}_{ij} + 2\sqrt{\frac{5}{6}} \beta \sqrt{S_n m^*} \boldsymbol{v}^n_{ij}, \quad \text{(A3)}$$

$$\boldsymbol{f}^t_{c,ij} = \begin{cases} -8G^*\sqrt{r^*\delta_n}\boldsymbol{t}_{ij} + 2\sqrt{\frac{5}{6}}\beta\sqrt{S_t m^*}\boldsymbol{v}^t_{ij} & \text{for } \left|\boldsymbol{f}^t_{c,ij}\right| < \mu_s \left|\boldsymbol{f}^n_{c,ij}\right|, \\ -\mu_s \left|\boldsymbol{f}^n_{c,ij}\right| \frac{\boldsymbol{t}_{ij}}{|\boldsymbol{t}_{ij}|} & \text{for } \left|\boldsymbol{f}^t_{c,ij}\right| \geq \mu_s \left|\boldsymbol{f}^n_{c,ij}\right|, \end{cases} \quad \text{(A4)}$$

where

$$\frac{1}{Y^*} = \frac{1-\nu_i^2}{Y_i} + \frac{1-\nu_j^2}{Y_j}, \quad \frac{1}{r^*} = \frac{1}{r_i} + \frac{1}{r_j}, \quad \text{(A5)}$$

$$\beta = \frac{\ln(e)}{\sqrt{\ln^2(e) + \pi^2}}, \quad S_n = 2Y^*\sqrt{r^*\delta_n}, \quad \text{(A6)}$$

$$\frac{1}{G^*} = \frac{2(2+\nu_i)(1-\nu_i)}{Y_i} + \frac{2(2+\nu_j)(1-\nu_j)}{Y_j}, \quad S_t = 8G^*\sqrt{r^*\delta_n}. \quad \text{(A7)}$$

The subscripts i and j denote spherical particles i and j, and the superscript $*$ denotes the effective particle property of those two particles. The effective particle mass m^* is calculated as $m^* = m_i m_j/(m_i + m_j)$; Y is Young's modulus; G is the shear modulus; ν is Poisson's ratio; r is the particle radius; δ_n is the normal overlap distance; $\boldsymbol{n}_{ij}$ represents the unit normal vector pointing from particle j to particle i; $\boldsymbol{v}^n_{ij}$ represents the normal velocity of particle j relative to particle i; $\boldsymbol{t}_{ij}$ represents the tangential displacement obtained from the integration of the relative tangential velocity during the contact, $\boldsymbol{v}^t_{ij}$; and μ_s is the particle sliding friction coefficient.

The van der Waals force $\mathbf{f}_{v,ik}$ between particles i and k is modeled as

$$\mathbf{f}_{v,ik} = -f_{v,ik}\mathbf{n}_{ik} = \begin{cases} -F_{\text{vdw}}(A,s)\mathbf{n}_{ik} & \text{for } s_{\min} < s < s_{\max}, \\ -F_{\text{vdw}}(A,s_{\min})\mathbf{n}_{ik} & \text{for } s \leq s_{\min}. \end{cases} \quad \text{(A8)}$$

Here, F_{vdw} is the magnitude of the van der Waals force between particles i and k given by Ref. 37 as

$$F_{\text{vdw}}(A,s) = \frac{A}{3}\frac{2r_i r_k (r_i + r_k + s)}{s^2(2r_i + 2r_k + s)^2} \times \left[\frac{s(2r_i + 2r_k + s)}{(r_i + r_k + s)^2 - (r_i - r_k)^2} - 1\right]^2, \quad \text{(A9)}$$

where A is the Hamaker constant which depends on the material properties[74] and s is the distance between the particle surfaces. It is assumed that the force saturates at a minimum separation distance, $s_{\min}$, which corresponds to typical intermolecular spacing.[75] This constant maximum force is also applied when the particles are in contact. As the magnitude of the van der Waals force decreases rapidly as the distance between the surfaces increases, a maximum cutoff distance $s_{\max} = (r_i + r_k)/4$[76] is employed to speed up the simulation. For $s > s_{\max}$, the van der Waals force is not accounted for.

To accelerate computations, simulations typically employ a soft Young's modulus (Y^S) that is much smaller than the real value (Y^R). The superscript S denotes that the parameter corresponds to the case where a soft Young's modulus is used, and the superscript R denotes that the parameters correspond to real particle properties. However, as shown previously,[28,31,61,77–79] this cohesion model, Eqs. (A9) and (A8), and the Johnson-Kendall-Roberts cohesion model[80] would yield simulation results that are dependent on Young's modulus of particles. Thus, a different cohesion model is requisite if one needs to soften the particles without significantly affecting the simulation results. A modified cohesion model has been developed[78] based on conserving cohesive energy to produce results that are insensitive to Young's modulus. This modified cohesion model is used in the simulations and shown below,

$$\mathbf{f}^M_{v,ik} = -f^M_{v,ik}\mathbf{n}_{ik} = \begin{cases} -F_{\text{vdw}}(A^R, s - s_o)\mathbf{n}_{ik} & \text{for } s^S_{\min} < s < s_{\max} \equiv (r_i + r_k)/4, \\ -F_{\text{vdw}}(A^S, s^R_{\min})\mathbf{n}_{ik} & \text{for } s \leq s^S_{\min} \end{cases} \quad \text{(A10)}$$

with A^S calculated by $A^S = A^R(Y^S/Y^R)^{2/5}$. The parameter $s^S_{\min}$ is the minimum separation distance for the soft Young's modulus and s_o is an additional model parameter. They can be found by solving the following equations:

$$F_{\text{vdw}}(\theta, s^R_{\min}) = F_{\text{vdw}}(1, s^S_{\min} - s_o), \quad \text{(A11)}$$

$$F_{\text{vdw}}(1, s^R_{\min})s^R_{\min} + \int_{s^R_{\min}}^{s_{\max}} F_{\text{vdw}}(1,s)ds = f_{v,ik}(\theta, s^R_{\min})s^S_{\min} + \int_{s^S_{\min}}^{s_{\max}} F_{\text{vdw}}(1, s - s_o)ds, \quad \text{(A12)}$$

where $s_{\max}$ is $(r_i + r_k)/4$ and θ is $(Y^S/Y^R)^{2/5}$.

The fluid phase is modeled by solving the following conservation of mass and momentum equations in terms of the locally averaged variables over a computational cell:

$$\frac{\partial}{\partial t}(1-\phi) + \boldsymbol{\nabla}\cdot\left[(1-\phi)\boldsymbol{u}_g\right] = 0, \quad \text{(A13)}$$

$$\rho_g(1-\phi)\left(\frac{\partial \boldsymbol{u}_g}{\partial t} + \boldsymbol{u}_g\cdot\boldsymbol{\nabla}\boldsymbol{u}_g\right) = -\boldsymbol{\nabla}p_g + \boldsymbol{\nabla}\cdot\boldsymbol{\tau}_g + \boldsymbol{\Phi}_d + \rho_g(1-\phi)\boldsymbol{g}. \quad \text{(A14)}$$

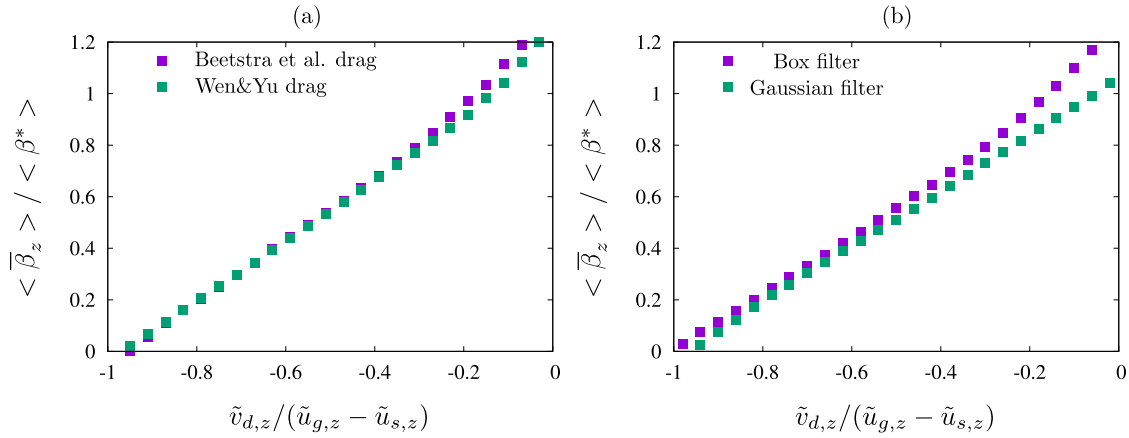

FIG. 13. Scaled filtered Eulerian drag coefficient as a function of the scaled drift velocity for (a) Wen and Yu[48] and Beetstra *et al.*[58] drag laws and (b) box and Gaussian filters with the Wen and Yu[48] drag law. The reference drag coefficient β^* is based on the filtered relative velocity and the filtered solid volume fraction. Domain-averaged solid volume fraction $\langle\phi\rangle = 0.1$; filtered volume fraction $\overline{\phi} = 0.1$; filter size $\Delta_f = 27\ d_p$.

Here, ρ_g is the density of the gas which is assumed to be constant, ϕ is the solid volume fraction, $\boldsymbol{u}_g$ is the gas velocity, p_g is the gas phase pressure, and $\boldsymbol{\tau}_g$ is the gas phase deviatoric stress tensor. The total gas-particle interaction force per unit volume of the mixture $-\boldsymbol{\Phi}_d$, exerted on the particles by the gas, is composed of a generalized buoyancy force due to the slowly varying (in space) local-average gas phase stress $(-p_g\boldsymbol{I} + \boldsymbol{\tau}_g)$ and the force due to the rapidly varying (in space) flow field around the particles.

In finite volume method-based computations employed in our simulations, $\boldsymbol{\Phi}_d$ in any computational cell is related to $\boldsymbol{f}_{g\to p,i}$ of all the particles in that cell as $\boldsymbol{\Phi}_d = -\frac{\sum_i^{cell} \boldsymbol{f}_{g\to p,i}}{V}$ where V is the volume of the computational cell. On a per particle basis, the total interaction force on the particle by the gas can be written as $\boldsymbol{f}_{g\to p,i} = -\mathcal{V}_{p,i}\boldsymbol{\nabla} p_g|_{\mathbf{x}=\mathbf{x}_{p,i}} + \mathcal{V}_{p,i}\boldsymbol{\nabla}\cdot\boldsymbol{\tau}_g|_{\mathbf{x}=\mathbf{x}_{p,i}} + \boldsymbol{f}_{d,i}$, where $\mathcal{V}_{p,i}$ is the particle volume and $\boldsymbol{f}_{d,i}$ is the drag force calculated by the Wen and Yu drag law.[48] Subscript i indicates that quantities are per particle and that fluid phase properties have been interpolated at the particle position, $|_{\mathbf{x}=\mathbf{x}_{p,i}}$. The gas phase deviatoric stress tensor contribution is relatively insignificant in $\boldsymbol{f}_{g\to p,i}$ for modeling gas-fluidized beds of particles[12] and hence ignored. The total interaction force is mapped on the Eulerian grid using a mollification kernel ξ characterized by a smoothing length equal to the mesh spacing Δ by following Ref. 81. The kernel function ξ is defined by

$$\xi(\mathcal{L}) = \begin{cases} \frac{1}{4}\mathcal{L}^4 - \frac{5}{8}\mathcal{L}^2 + \frac{115}{192}, & \text{if } \mathcal{L} \le 0.5, \\ -\frac{1}{6}\mathcal{L}^4 + \frac{5}{6}\mathcal{L}^3 - \frac{5}{4}\mathcal{L}^2 + \frac{5}{24}\mathcal{L} + \frac{55}{96}, & \text{if } 0.5 < \mathcal{L} \le 1.5, \\ \frac{(2.5-\mathcal{L})^4}{24}, & \text{if } 1.5 < \mathcal{L} \le 2.5, \\ 0, & \text{otherwise,} \end{cases} \tag{A15}$$

where the symbol $\mathcal{L} = d/\Delta$ and d is the distance from the particle position $\mathbf{x}_{p,i}$ to face center coordinate $\mathbf{x}$. The total force is mapped over the 27 nearest cells around the particle location. The fluid variables at the particle position are computed by a linear interpolation using the distance weightings $\mathcal{L}$.

APPENDIX B: EFFECT OF FILTER TYPE AND MICROSCOPIC DRAG LAW

Figure 13(a) shows the variation of the scaled filtered drag with the scaled drift velocity for Wen and Yu[48] and Beetstra *et al.*[58] drag laws for $\Delta_f = 27\ d_p$ and $\overline{\phi} = 0.1$. In these simulations, the domain size is $180\,d_p \times 180\,d_p \times 720\,d_p$ with a particle diameter of 145 μm and domain-averaged solid volume fraction $\langle\phi\rangle$ of 0.1. It shows that the dependency of the scaled filtered drag on the scaled drift velocity is independent of the choice of the microscopic drag law.

To study the effect of filter type on the filtered drag coefficient, we also explored the use of a Gaussian filter to compute the scaled drag coefficient and the scaled drift velocity. The polynomial function approximation of a continuous Gaussian function[81] [see Eq. (A15)] was used to compute the weights of the filtering kernel. We used a limited number of neighboring cells n_{cell} instead of looping over all cells in the domain to avoid excessive computational expense. The limited number of neighboring cells n_{cell} is given by $(\Delta_f/\Delta)^3$.

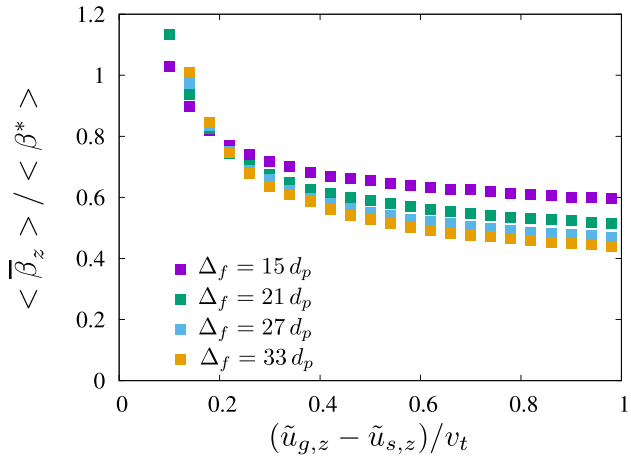

FIG. 14. Scaled filtered Eulerian drag coefficient as a function of the scaled relative velocity for various filter sizes. The reference drag coefficient β^* is based on the filtered relative velocity and the filtered solid volume fraction. Domain-averaged solid volume fraction $\langle\phi\rangle = 0.1$; filtered volume fraction $\overline{\phi} = 0.1$; Froude number 65. Simulation parameters are summarized in Table I.

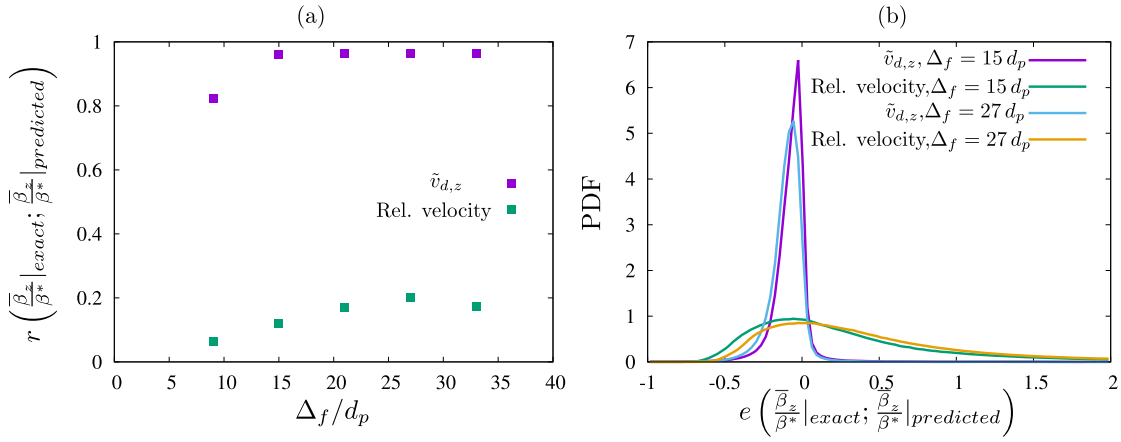

FIG. 15. (a) Pearson correlation coefficients between exact and predicted drag coefficients using the drift velocity and the relative velocity model for various filter sizes. (b) Probability distribution function of the relative error between exact and predicted drag coefficients using the drift velocity and the relative velocity model for filter sizes, $\Delta_f = 15\ d_p$ and $27\ d_p$. The reference drag coefficient β^* is based on the filtered relative velocity and the filtered solid volume fraction. Domain-averaged solid volume fraction $\langle\phi\rangle = 0.1$; Froude number 65. Simulation parameters are summarized in Table I.

Figure 13(b) shows the scaled drag coefficient as a function of the scaled drift velocity with box and Gaussian filters for $\Delta_f = 27\ d_p$ and $\overline{\phi} = 0.1$. This result shows that departure from linear relationship is less significant with a Gaussian filter. Thus, the choice of a filter has a small effect on the closure model, which is not surprising in a problem with multi-scale structures. Why a Gaussian filter would offer a more linear relation than a box filter will be explored in a future study. This comparison clearly emphasizes that one should adopt a consistent choice of filters in both model formulation and subsequent application.

APPENDIX C: ASSESSMENT OF EFFECTIVE DRAG MODELING USING FILTERED QUANTITIES

Igci and Sundaresan[20] correlated the scaled drag coefficient for a chosen filter size using only $\overline{\phi}$ as a marker. Several authors[22,23,26] included the filtered relative velocity, $\tilde{u}_{g,i} - \tilde{u}_{s,i}$, as an additional marker in their correlations. These models did not adjust any parameters dynamically via a scale similarity approach [unlike Eq. (16) above where κ is determined dynamically]. Ozarkar *et al.*[82] compared the predictions of filtered two-fluid model simulations with experimental data and found that including the filtered relative velocity as an additional marker led to a significant improvement in the predictions. Figure 14 shows the variation of the scaled drag coefficient with the scaled relative velocity for different filter sizes and one particular $\overline{\phi}$; these results were extracted by post-processing the snapshots from a simulation with non-cohesive particles with $Fr_p = 65$. Similar results are obtained for other filtered solid volume fractions as well.

A look-up table was created using these results (at each filter size) through an artificial neural network scheme. This look-up table was then used to determine the Pearson correlation coefficient for each filter size. Figure 15(a) shows the Pearson coefficients for several different filter sizes, while Fig. 15(b) shows the PDFs for two filter sizes. For comparison, these figures also include the results for the drift velocity approach [which were presented in Figs. 11(a) and 11(b)]. It is clear that the drift velocity is considerably superior; estimating the drift velocity via a scale similarity method (Fig. 12) is still much better than explicit use of the filtered relative velocity as a marker. It seems reasonable to conclude that the dynamic adjustment plays an important role in affording superior predictions.

[1] B. J. Glasser, S. Sundaresan, and I. G. Kevrekidis, "From bubbles to clusters in fluidized beds," Phys. Rev. Lett. **81**, 1849–1852 (1998).
[2] D. Geldart, "Types of gas fluidization," Powder Technol. **7**, 285–292 (1973).
[3] O. Molerus, "Interpretation of Geldart's type A, B, C and D powders by taking into account interparticle cohesion forces," Powder Technol. **33**, 81–87 (1982).
[4] T. B. Anderson and R. Jackson, "Fluid mechanical description of fluidized beds. Equations of motion," Ind. Eng. Chem. Fundam. **6**, 527–539 (1967).
[5] C. K. K. Lun, S. B. Savage, D. J. Jeffrey, and N. Chepurniy, "Kinetic theories for granular flow: Inelastic particles in Couette flow and slightly inelastic particles in a general flow field," J. Fluid Mech. **140**, 223–256 (1984).
[6] D. Gidaspow, *Multiphase Flow and Fluidization: Continuum and Kinetic Theory Descriptions*, 1st ed. (Academic Press, Boston, 1994).
[7] G. Balzer, A. Boelle, and O. Simonin, "Eulerian gas-solid flow modelling of dense fluidized bed," in *Fluidization VIII—Proceedings of the International Symposium of Engineering Foundation*, edited by J. F. Large and C. Laguérie (Engineering Foundation, 1998), pp. 1125–1134.
[8] D. L. Koch and A. S. Sangani, "Particle pressure and marginal stability limits for a homogeneous monodisperse gas-fluidized bed: Kinetic theory and numerical simulations," J. Fluid Mech. **400**, 229–263 (1999).
[9] V. Garzó and J. W. Dufty, "Dense fluid transport for inelastic hard spheres," Phys. Rev. E **59**, 5895–5911 (1999).
[10] V. Garzó, S. Tenneti, S. Subramaniam, and C. M. Hrenya, "Enskog kinetic theory for monodisperse gas-solid flows," J. Fluid Mech. **712**, 129–168 (2012).
[11] L. L. Yang, J. T. J. Padding, and J. A. M. H. Kuipers, "Modification of kinetic theory of granular flow for frictional spheres. Part I: Two-fluid model derivation and numerical implementation," Chem. Eng. Sci. **152**, 767–782 (2016).
[12] K. Agrawal, P. N. Loezos, M. Syamlal, and S. Sundaresan, "The role of meso-scale structures in rapid gas-solid flows," J. Fluid Mech. **445**, 151–185 (2001).
[13] W. Wang and J. Li, "Simulation of gas–solid two-phase flow by a multi-scale CFD approach–of the EMMS model to the sub-grid level," Chem. Eng. Sci. **62**, 208–231 (2007).
[14] A. Ozel, P. Fede, and O. Simonin, "Development of filtered Euler-Euler two-phase model for circulating fluidised bed: High resolution simulation, formulation and a priori analyses," Int. J. Multiphase Flow **55**, 43–63 (2013).
[15] H. Weinstein, M. Shao, and L. Wasserzug, "Radial solid density variation in a fast fluidized bed," in *AIChE Symposium Series (United States)* (Department of Chemical Engineering, The City College of the City University of New York, New York, NY, 1984), Vol. 80.

[16]J. Wang, M. A. van der Hoef, and J. A. M. Kuipers, "Why the two-fluid model fails to predict the bed expansion characteristics of Geldart a particles in gas-fluidized beds: A tentative answer," Chem. Eng. Sci. **64**, 622–625 (2009).
[17]W. D. Fullmer and C. M. Hrenya, "Quantitative assessment of fine-grid kinetic-theory-based predictions of mean-slip in unbounded fluidization," AIChE J. **62**, 11–17 (2016).
[18]W. D. Fullmer and C. M. Hrenya, "The clustering instability in rapid granular and gas-solid flows," Annu. Rev. Fluid Mech. **49**, 485–510 (2017).
[19]Y. Igci, A. T. Andrews, S. Sundaresan, S. Pannala, and T. O'Brien, "Filtered two-fluid models for fluidized gas-particle suspensions," AIChE J. **54**, 1431–1448 (2008).
[20]Y. Igci and S. Sundaresan, "Constitutive models for filtered two-fluid models of fluidized gas-particle flows," Ind. Eng. Chem. Res. **50**, 13190–13201 (2011).
[21]J.-F. Parmentier, O. Simonin, and O. Delsart, "A functional subgrid drift velocity model for filtered drag prediction in dense fluidized bed," AIChE J. **58**, 1084–1098 (2012).
[22]C. C. Milioli, F. E. Milioli, W. Holloway, K. Agrawal, and S. Sundaresan, "Filtered two-fluid models of fluidized gas-particle flows: New constitutive relations," AIChE J. **59**, 3265–3275 (2013).
[23]S. Schneiderbauer and S. Pirker, "Filtered and heterogeneity-based subgrid modifications for gas-solid drag and solid stresses in bubbling fluidized beds," AIChE J. **60**, 839–854 (2014).
[24]S. Schneiderbauer, "A spatially-averaged two-fluid model for dense large-scale gas-solid flows," AIChE J. **63**, 3544–3562 (2017).
[25]M. Moreau, O. Simonin, and B. Bédat, "Development of gas-particle Euler-Euler LES approach: A priori analysis of particle sub-grid models in homogeneous isotropic turbulence," Flow, Turbul. Combust. **84**, 295–324 (2009).
[26]A. Sarkar, F. E. Milioli, S. Ozarkar, T. Li, X. Sun, and S. Sundaresan, "Filtered sub-grid constitutive models for fluidized gas-particle flows constructed from 3-D simulations," Chem. Eng. Sci. **152**, 443–456 (2016).
[27]M. H. Zhang, K. W. Chu, F. Wei, and A. B. Yu, "A CFD-DEM study of the cluster behavior in riser and downer reactors," Powder Technol. **184**, 151–165 (2008).
[28]T. Kobayashi, T. Tanaka, N. Shimada, and T. Kawaguchi, "DEM-CFD analysis of fluidization behavior of Geldart group A particles using a dynamic adhesion force model," Powder Technol. **248**, 143–152 (2013).
[29]M. W. Korevaar, J. T. Padding, M. A. Van der Hoef, and J. A. M. Kuipers, "Integrated DEM-CFD modeling of the contact charging of pneumatically conveyed powders," Powder Technol. **258**, 144–156 (2014).
[30]Y. Gu, A. Ozel, and S. Sundaresan, "Numerical studies of the effects of fines on fluidization," AIChE J. **62**, 2271–2281 (2016).
[31]P. Liu, C. Q. LaMarche, K. M. Kellogg, and C. M. Hrenya, "Fine-particle defluidization: Interaction between cohesion, Young's modulus and static bed height," Chem. Eng. Sci. **145**, 266–278 (2016).
[32]M. Girardi, S. Radl, and S. Sundaresan, "Simulating wet gas-solid fluidized beds using coarse-grid CFD-DEM," Chem. Eng. Sci. **144**, 224–238 (2016).
[33]C. M. Boyce, A. Ozel, J. Kolehmainen, S. Sundaresan, C. A. McKnight, and M. Wormsbecker, "Growth and breakup of a wet agglomerate in a dry gas-solid fluidized bed," AIChE J. **63**, 2520–2527 (2017).
[34]C. M. Boyce, A. Ozel, J. Kolehmainen, and S. Sundaresan, "Analysis of the effect of small amounts of liquid on gas-solid fluidization using CFD-DEM simulations," AIChE J. (published online 2017).
[35]J. Kolehmainen, A. Ozel, C. M. Boyce, and S. Sundaresan, "Triboelectric charging of monodisperse particles in fluidized beds," AIChE J. **63**, 1872–1891 (2017).
[36]A. Ozel, J. Kolehmainen, S. Radl, and S. Sundaresan, "Fluid and particle coarsening of drag force for discrete-parcel approach," Chem. Eng. Sci. **155**, 258–267 (2016).
[37]H. C. Hamaker, "The London—van der Waals attraction between spherical particles," Physica **4**, 1058–1072 (1937).
[38]OpenFOAM, OpenFOAM 2.2.2, User Manual, 2013.
[39]C. Kloss, C. Goniva, and Minerals, Metals, and Materials Society, "LIGGGHTS—Open source discrete element simulations of granular materials based on Lammps," in *Supplemental Proceedings: Materials Fabrication, Properties, Characterization, and Modeling* (John Wiley & Sons, Inc., 2011), pp. 781–788.
[40]C. Kloss, C. Goniva, A. Hager, S. Amberger, and S. Pirker, "Models, algorithms and validation for opensource DEM and CFD–DEM," Prog. Comput. Fluid Dyn. Int. J. **12**, 140–152 (2012).
[41]C. Goniva, C. Kloss, N. G. Deen, J. A. M. Kuipers, and S. Pirker, "Influence of rolling friction on single spout fluidized bed simulation," Particuology **10**, 582–591 (2012).
[42]P. A. Cundall and O. D. L. Strack, "A discrete numerical model for granular assemblies," Géotechnique **29**, 47–65 (1979).
[43]W. C. Swope, H. C. Andersen, P. H. Berens, and K. R. Wilson, "A computer simulation method for the calculation of equilibrium constants for the formation of physical clusters of molecules: Application to small water clusters," J. Chem. Phys. **76**, 637–649 (1982).
[44]V. Mathiesen, T. Solberg, H. Arastoopour, and B. H. Hjertager, "Experimental and computational study of multiphase gas/particle flow in a CFB riser," AIChE J. **45**, 2503–2518 (1999).
[45]P. Lettieri, D. Newton, and J. G. Yates, "Homogeneous bed expansion of FCC catalysts, influence of temperature on the parameters of the Richardson–Zaki equation," Powder Technol. **123**, 221–231 (2002).
[46]T. Li, S. Rabha, V. Verma, J.-F. Dietiker, Y. Xu, L. Lu, W. Rogers, B. Gopalan, G. Breault, J. Tucker, and R. Panday, "Experimental study and discrete element method simulation of Geldart group A particles in a small-scale fluidized bed," Adv. Powder Technol. **28**, 2961–2973 (2017).
[47]S. Radl and S. Sundaresan, "A drag model for filtered Euler-Lagrange simulations of clustered gas-particle suspensions," Chem. Eng. Sci. **117**, 416–425 (2014).
[48]C. Wen and Y. Yu, "Mechanics of fluidization," Chem. Eng. Prog. Symp. Ser. **62**, 100–111 (1966).
[49]R. O. Fox, "On multiphase turbulence models for collisional fluid-particle flows," J. Fluid Mech. **742**, 368–424 (2014).
[50]J. Capecelatro, O. Desjardins, and R. O. Fox, "On fluid-particle dynamics in fully developed cluster-induced turbulence," J. Fluid Mech. **780**, 578–635 (2015).
[51]J. Capecelatro, O. Desjardins, and R. O. Fox, "Strongly coupled fluid-particle flows in vertical channels. I. Reynolds-averaged two-phase turbulence statistics," Phys. Fluids **28**, 033306 (2016).
[52]C. D. Pierce and P. Moin, "A dynamic model for subgrid-scale variance and dissipation rate of a conserved scalar," Phys. Fluids **10**, 3041–3044 (1998).
[53]G. Balarac, H. Pitsch, and V. Raman, "Development of a dynamic model for the subfilter scalar variance using the concept of optimal estimators," Phys. Fluids **20**, 035114 (2008).
[54]E. Knudsen, E. S. Richardson, E. M. Doran, H. Pitsch, and J. H. Chen, "Modeling scalar dissipation and scalar variance in large eddy simulation: Algebraic and transport equation closures," Phys. Fluids **24**, 055103 (2012).
[55]C. Jiménez, F. Ducros, B. Cuenot, and B. Bédat, "Subgrid scale variance and dissipation of a scalar field in large eddy simulations," Phys. Fluids **13**, 1748–1754 (2001).
[56]J. Capecelatro, O. Desjardins, and R. O. Fox, "Strongly coupled fluid-particle flows in vertical channels. II. Turbulence modeling," Phys. Fluids **28**, 033307 (2016).
[57]J. Capecelatro, O. Desjardins, and R. O. Fox, "Effect of domain size on fluid-particle statistics in homogeneous, gravity-driven, cluster-induced turbulence," J. Fluids Eng. **138**, 041301–8 (2015).
[58]R. Beetstra, M. A. van der Hoef, and J. A. M. Kuipers, "Drag force of intermediate Reynolds number flow past mono- and bidisperse arrays of spheres," AIChE J. **53**, 489–501 (2007).
[59]A. Castellanos, J. M. Valverde, and M. A. S. Quintanilla, "Aggregation and sedimentation in gas-fluidized beds of cohesive powders," Phys. Rev. E **64**, 041304 (2001).
[60]J. M. Valverde, A. Castellanos, and M. A. Sanchez Quintanilla, "Self-diffusion in a gas-fluidized bed of fine powder," Phys. Rev. Lett. **86**, 3020–3023 (2001).
[61]R. Wilson, D. Dini, and B. van Wachem, "A numerical study exploring the effect of particle properties on the fluidization of adhesive particles," AIChE J. **62**, 1467–1477 (2016).
[62]D. L. Marchisio, R. D. Vigil, and R. O. Fox, "Quadrature method of moments for aggregation–breakage processes," J. Colloid Interface Sci. **258**, 322–334 (2003).
[63]D. L. Marchisio, J. T. Pikturna, R. O. Fox, R. D. Vigil, and A. A. Barresi, "Quadrature method of moments for population-balance equations," AIChE J. **49**, 1266–1276 (2003).
[64]D. L. Marchisio and R. O. Fox, *Computational Models for Polydisperse Particulate and Multiphase Systems* (Cambridge University Press, 2013).
[65]H. Arastoopour, "Numerical simulation and experimental analysis of gas/solid flow systems: 1999 Fluor-Daniel Plenary lecture," Powder Technol. **119**, 59–67 (2001).

[66]H. Kim and H. Arastoopour, "Extension of kinetic theory to cohesive particle flow," Powder Technol. **122**, 83–94 (2002).
[67]H. Seu-Kim and H. Arastoopour, "Simulation of FCC particles flow behavior in a CFB using modified kinetic theory," Can. J. Chem. Eng. **73**, 603–611 (1995).
[68]S. H. L. Kriebitzsch, M. A. van der Hoef, and J. A. M. Kuipers, "Drag force in discrete particle models-continuum scale or single particle scale?," AIChE J. **59**, 316–324 (2013).
[69]G. Zhou, Q. Xiong, L. Wang, X. Wang, X. Ren, and W. Ge, "Structure-dependent drag in gas–solid flows studied with direct numerical simulation," Chem. Eng. Sci. **116**, 9–22 (2014).
[70]T. Li, L. Wang, W. Rogers, G. Zhou, and W. Ge, "An approach for drag correction based on the local heterogeneity for gas–solid flows," AIChE J. **63**, 1203–1212 (2017).
[71]G. J. Rubinstein, A. Ozel, Y. Xiaolong, J. J. Derksen, and S. Sundaresan, "Lattice Boltzmann simulations of low-Reynolds-number flows past fluidized spheres: Effect of inhomogeneities on the drag force," J. Fluid Mech. (to be published).
[72]K. L. Johnson and K. L. Johnson, *Contact Mechanics* (Cambridge University Press, 1987).
[73]A. Di Renzo and F. P. Di Maio, "Comparison of contact-force models for the simulation of collisions in DEM-based granular flow codes," Chem. Eng. Sci. **59**, 525–541 (2004).
[74]J. N. Israelachvili, *Intermolecular and Surface Forces* (Academic Press, 2015).
[75]R. Y. Yang, R. P. Zou, and A. B. Yu, "Computer simulation of the packing of fine particles," Phys. Rev. E **62**, 3900–3908 (2000).
[76]L. Aarons and S. Sundaresan, "Shear flow of assemblies of cohesive and non-cohesive granular materials," Powder Technol. **169**, 10–21 (2006).
[77]R. Moreno-Atanasio, B. H. Xu, and M. Ghadiri, "Computer simulation of the effect of contact stiffness and adhesion on the fluidization behaviour of powders," Chem. Eng. Sci. **62**, 184–194 (2007).
[78]Y. Gu, A. Ozel, and S. Sundaresan, "A modified cohesion model for CFD-DEM simulations of fluidization," Powder Technol. **296**, 17–28 (2016).
[79]E. Murphy and S. Subramaniam, "Binary collision outcomes for inelastic soft-sphere models with cohesion," Powder Technol. **305**, 462–476 (2017).
[80]J. Haervig, U. Kleinhans, C. Wieland, H. Spliethoff, A. L. Jensen, K. Sørensen, and T. J. Condra, "On the adhesive JKR contact and rolling models for reduced particle stiffness discrete element simulations," Powder Technol. **319**, 472 (2017).
[81]P. Pepiot and O. Desjardins, "Numerical analysis of the dynamics of two- and three-dimensional fluidized bed reactors using an Euler–Lagrange approach," Powder Technol. **220**, 104–121 (2012).
[82]S. S. Ozarkar, X. Yan, S. Wang, C. C. Milioli, F. E. Milioli, and S. Sundaresan, "Validation of filtered two-fluid models for gas–particle flows against experimental data from bubbling fluidized bed," Powder Technol. **284**, 159–169 (2015).